FACULTY
OF MATHEMATICS
AND PHYSICS
Charles University

MASTER THESIS

Marcel Štolc

Accretion discs in the context of tidal disruption of stars in nuclei of galaxies

Astronomical Institute of the Charles University in Prague

Supervisor of the master thesis: prof. RNDr. Vladimír Karas, DrSc.

Study programme: Physics

Study branch: Astronomy and Astrophysics

Prague 2019

I declare that I carried out this master thesis independently, and only with the cited sources, literature and other professional sources.

I understand that my work relates to the rights and obligations under the Act No. 121/2000 Sb., the Copyright Act, as amended, in particular the fact that the Charles University has the right to conclude a license agreement on the use of this work as a school work pursuant to Section 60 subsection 1 of the Copyright Act.

In Prague, 6 May 2019

Title: Accretion discs in the context of tidal disruption of stars in nuclei of galaxies

Author: Marcel Štolc

Department: Astronomical Institute of the Charles University in Prague

Supervisor: prof. RNDr. Vladimír Karas, DrSc., Astronomical Institute of the Czech Academy of Sciences

Abstract: Stars can be stretched and ripped apart by the super-massive black hole at the core of a galaxy. The remnant gaseous trail gradually circularizes in a ring of mass that spreads by the viscous forces into an accretion disc. In this thesis we have studied the spectral line profile time evolution of radiation reflected by the accretion disc located around a super-massive black hole. We assume the central body to be a slowly rotating or non-rotating super-massive black hole with no charge, in the first approximation represented by the Schwarzschild solution. In a sense of Shakura-Sunyaev standard accretion disc model with the kinematic viscosity parameter $\alpha \approx 1$ we allow the accretion disc evolution to be guided by the angular momentum transfer equation with the initial mass ring located at the tidal radius being the product of tidal disruption of a star passing by a super-massive black hole. During the simulations we keep varying the mass of the central body while we keep the mass and the radius of the star constant ($M = 1 M_\odot$ and $R = 1 R_\odot$), i.e. taking into account the solar-type stars only. We defer the prospects of the full analysis involving spin (and charge) of the central body for the future study as it will be necessary to use the equations for the redshift factor and the accretion disc evolution that correspond to the Kerr (or Kerr-Newmann) metric.

Keywords: Galaxy – black holes – accretion discs – radiation

Název práce: Akreční disky v kontextu slapového trhání hvězd v jádrech galaxií

Autor: Marcel Štolc

Katedra: Astronomický ústav Univerzity Karlovy v Praze

Vedoucí diplomové práce: prof. RNDr. Vladimír Karas, DrSc., Astronomický ústav Akademie věd České republiky

Abstrakt: Hvězdy mohou být protaženy a roztrhány super-masivní černou dírou v jádru galaxie. Zbytková plynná stopa postupně cirkularizuje v hmotnostní prstenec, který se působením viskózních sil vyvíjí v akreční disk. V této práci jsme studovali evoluci časových profilů spektrálních čar záření odraženého akrečním diskem umístěným kolem super-masivní černé díry. Předpokládáme, že centrální těleso bude pomalu rotující nebo nerotující super-masivní černá díra bez náboje, v první aproximaci reprezentovaná Schwarzschildovym řešením. Ve smyslu modelu Shakura-Sunayevova standardního akrečního disku s parametrem kinematické viskozity $\alpha \approx 1$ povolíme akrečnímu disku vyvíjet se podle rovnice přenosu momentu hybnosti s počátečním hmotnostním prstencem umístěným na slapovém poloměru, který je výsledkem slapového trhání hvězdy prolétávající kolem super-masivní černé díry. Během simulací měníme hmotnost centrálního tělesa, zatímco hmotu a poloměr hvězdy udržujeme konstantní ($M = 1M_\odot$ and $R = 1R_\odot$), tj. bereme v úvahu jen hvězdy slunečního typu. Odkládáme vyhlídky plné analýzy zahrnující spin (a náboj) centrálního telesa pro budoucí studium, protože bude nutné použít rovnice pro posun frekvence a evoluce akrečního disku, které odpovídají Kerrově (nebo Kerr-Newmannově) metrice.

Klíčová slova: Galaxie – černé díry – akreční disky – záření
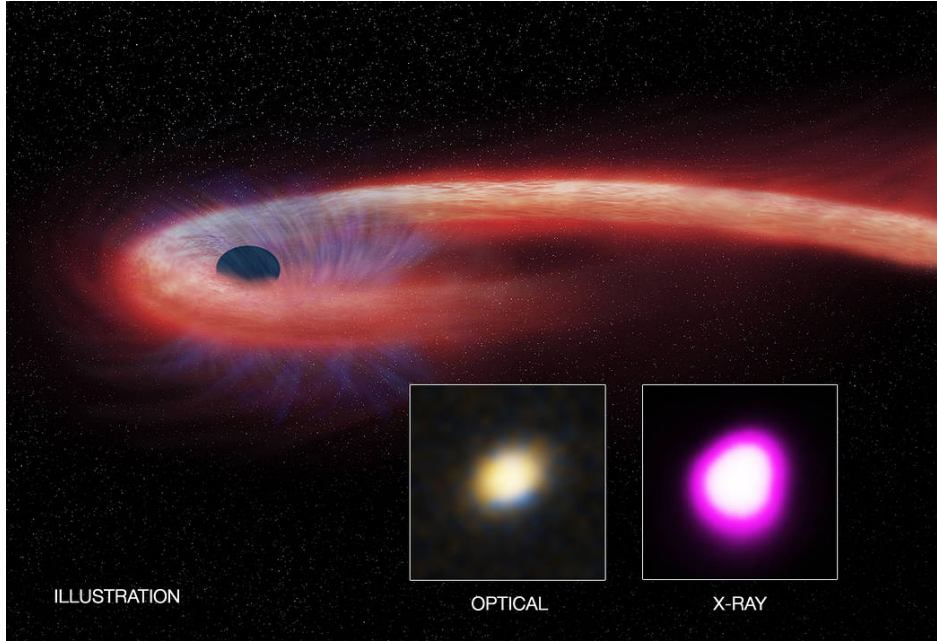
Contents

Introduction

Figure 1: Artist's illustration of TDE and the idea of the mechanism producing subsequent spectral features by the illumination of the remnant material embedded in the hot accreting environment. This scenario has been motivated by the actual event XJ1500+0154 reported in X-ray and optical observations (see further details in the subsequent sections). Image credit: Illustration: CXC/M. Weiss; X-ray: NASA/CXC/UNH/[Lin et al., 2017], Optical: CFHT.

Tidal disruption events (TDEs) are transient phenomena that are caused by the process of abrupt damage to a star approaching and transiting a critical distance from a compact gravitating body, presumably a super-massive black hole $(10^5 M_\odot \lesssim M \lesssim 10^8 M_\odot)$ in the core of a galaxy or a massive black hole $(M \simeq 10^3$–$10^4 M_\odot)$ in a globular cluster. TDEs are caused by large difference of the gravitational field that acts over the size of the star, as the gradient of the gravitational force overcomes the star self-gravity and rips its body apart. The efficiency of the process depends critically on the compactness of both the challenged star and the acting (super-)massive black hole: more massive stars very close to less massive black holes are increasingly prone to the disruption. Such episodes lead to the increase of the mass accretion rate and the enhancement of the radiation emerging temporarily in the form of a flare in X-ray band and in other wavelengths (see Figure 1). The flaring TDE objects give us an opportunity to probe the environment of galactic nuclei and to determine their parameters, namely to constrain its size, the mass and the angular momentum (spin) of its central body.

The number of TDE candidates grows as they are found serendipitously during the slew surveys as sudden, unexpected rebrightening in the spectra in contrast with for a longer time observed, rapidly changing X-ray spectra of active galactic nuclei (AGN). TDE vary in different ways over the timescale of the process, but their typical signpost is the bolometric luminosity decrease as $\approx$ $t^{-\frac{5}{3}}$. However there are a couple observations of TDEs suggesting challenging

interpretations. [Liu et al., 2009, 2014] show that in case of an additional black hole present in the system the bolometric luminosity decrease as $\approx t^{-\frac{5}{3}}$ is no longer the case. They argue with the help of numerical simulations closely matching the observed data that the second super-massive black hole causes the lightcurve to be broken as it feeds on the accretion flow, when passing around the other one. [Cummings et al., 2011] points out there is a possibility of a jet formation in systems that are undergoing the early phases of tidal disruption. Based on the data of the same observation [Kara et al., 2016] propose Fe Kα emission line in a highly ionized state to be present in the spectra.

As a motivation (albeit tentative and indirect) we mention two crucial observational results that provide us with the evidence about the operation of accretion mechanism onto super-massive black holes in galactic nuclei and the emerging spectral features (see Figure 2 – 3). The current evidence about super-massive black holes in great majority concerns AGN for obvious reasons: active galaxies are very bright in the electromagnetic window and they are this more easily accessible to our observational techniques over the entire spectrum.

Figure 2 shows the interferometric image obtained recently by the Event Horizon Telescope (EHT). The image of the core of the giant elliptical galaxy M 87 is broadly consistent with theoretical predictions, in particular, the compact dark shadow that has been revealed in the core at significant dynamical range reaching the contrast ~ 50.

Figure 3 shows the X-ray spectrum of the Seyfert galaxy MCG 6-30-15 of kiloelectronvolt range. The spectrum exhibits the skewed and redshifted profile of the reflection line of iron (corresponding to Kα transition), consistent with the scenario of super-massive black hole disc accretion.

In this diploma thesis we intend to study the effects of general relativity around a super-massive black hole located at the galactic centre making itself noticeable in the spectra of the strongest spectral lines such as Fe Kα line with energy ≈ 6.4 keV. The strength of line combined with strong gravity in the close proximity of a super-massive black hole allows to observe not only the Doppler shift due to the rapid velocity of orbiting debris but also the gravitational redshift and the light bending effect. Whereas TDEs are frequently associated with inactive galaxies in quiescent state (see e.g. [Saxton et al., 2012], further details in the subsequent sections) we anticipate the emergence of X-ray spectral features in future observations of TDEs. With this outlook we study the expected spectral features.

We aim to model the time evolution of a spectral line profile incipient due to the interaction of corona, a high-energetic medium surrounding the galactic nucleus, and the evolving accretion disc with a slowly rotating or non-rotating super-massive black hole, i.e. approximated by the Schwarzschild solution, at its centre. In the first chapter we describe the concept of tidal radius and tidal disruption that would "generate" the initial mass ring. We also mention the key equations describing the steady state thin accretion disc model, the Shakura-Sunyaev standard accretion disc model, as well as the emission line and the redshift properties of observed radiation. The second chapter concerns the results of numerical integration of the angular momentum transfer equation (diffusion equation), i.e. the surface density structure of the accretion disc, the spectral line profiles of radiating gaseous rings and accretion discs, and the time evolution

of spectral line profile of radiation reflected by the evolving accretion disc. In the third chapter we summarize, contemplate our results, and we provide future prospects of the study. We defer the prospects of constraining the spin of the black hole to future work when the full Kerr metric is taken into account.
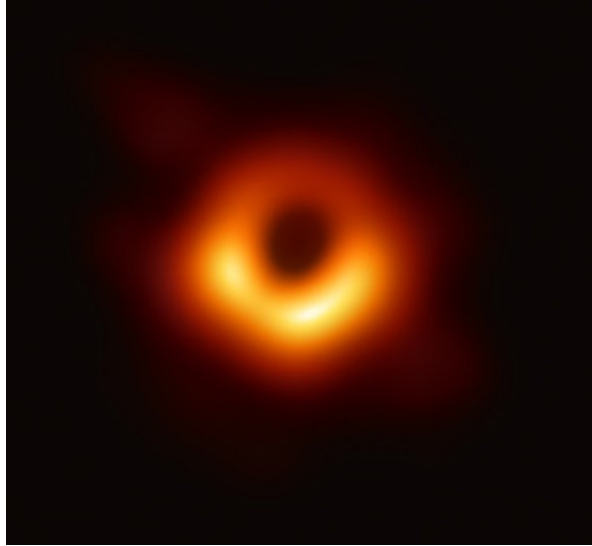

Figure 2: A shadow-picture of super-massive black hole located at the centre of galaxy M 87 with a randomly distributed photons coming from the accretion disc surrounding it. Image Credit: [Event Horizon Telescope Collaboration et al., 2019].
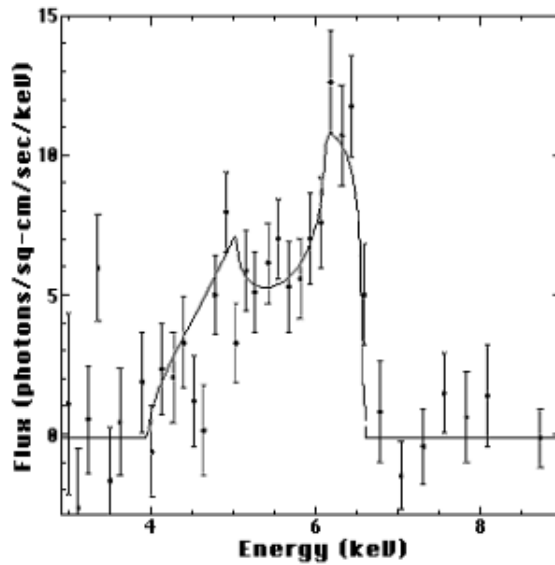

Figure 3: Energy excess indicating Fe Kα emission in the spectra of MCG 6-30-15. Image Credit [Tanaka et al., 1995].

1. Theory

1.1 Tidal disruption of a star − basic relations

The classical gravitational interaction of two point-like bodies is described by the Newtonian formula

$$F^i = -\frac{GMm}{R^3}R^i = -\frac{GMm}{R^2}\hat{R}^i, \tag{1.1}$$

where G stands for the gravitational constant, R^i is the i-th component of the vector pointing from the body of mass M to the other body of mass m gravitationally interacting with each other, and $\hat{R}^i$ is normalized version of R^i attained by dividing R^i by $\|R\| = \|R^i{}_i\|$ whereas $i = 1, 2, 3$. The resulting gravitational acceleration of the test mass m by the body M ($m \ll M$) is then described as

$$a^i = -\frac{GM}{R^2}\hat{R}^i. \tag{1.2}$$

When studying the gravitational acceleration let us introduce an infinitesimal displacement δR ($\delta R \ll R$) so that we can rewrite the equation (1.2) as follows

$$a^i = -\frac{GM}{(R \pm \delta R)^2}\hat{R}^i = -\frac{GM}{(1 \pm \frac{\delta R}{R})^2}\frac{\hat{R}^i}{R^2}. \tag{1.3}$$

Now taking into account $\delta R \ll R$ we can rewrite the equation (1.3) using Taylor expansion as

$$a^i = -\frac{GM\hat{R}^i}{R^2}\Big(1 \mp 2\frac{\delta R}{R} + O\Big(\frac{\delta R^2}{R^2}\Big)\Big). \tag{1.4}$$

Neglecting the second order of "the displacement to position term" we are presented with an additional term describing the components of tidal acceleration a_{tidal}^i

$$a_{\text{tidal}}^i = \pm\frac{2GM\delta R}{R^3}\hat{R}^i. \tag{1.5}$$

For our purposes let us set the mass of the body M to be the mass of a black hole M_{BH}, mass m to be the mass of a star M_* and δR to R_* as the radius of a star. Significant tidal force is the primary characteristic a compact object, especially the cosmic black holes. Setting the tidal force of black hole equal to the self-gravity of the star (still assuming the purely Newtonian framework, neglecting the effects of general relativity)

$$\left|\pm\frac{2GM_{\text{BH}}M_*R_*}{R^3}\right| = \left|-\frac{GM_*^2}{R_*^2}\right| \tag{1.6}$$

gives us the limit for the distance at which the star is able to withstand the gravitational pull exerted on its different parts by the black hole (or in general a way more massive compact object than the star itself). Such a distance has been called the tidal radius, R_{tidal} [Hills, 1975, Rees, 1988]. R_{tidal} depends on M_{BH}, M_* and R_* as follows

$$R_{\text{tidal}} = \Big(\frac{2M_{\text{BH}}}{M_*}\Big)^{\frac{1}{3}}R_*. \tag{1.7}$$

We thus ignore the time evolution of black hole mass and set it to be constant on the viscous timescale as the initial approximation. The tidal radius R_{tidal} scales as $\propto M_{\text{BH}}^{\frac{1}{3}}$ whereas the gravitational radius, R_{g} defined as

$$R_{\text{g}} = \frac{GM}{c^2}, \tag{1.8}$$

scales as $\propto M_{\text{BH}}$. That leads to the conclusion that there has to be a limiting mass for the black hole's capability to tidally strip or disrupt a star. This limiting mass, i.e. the Hills mass M_{Hills}, is given as

$$M_{\text{Hills}} = 1.1 \times 10^8 M_\odot \left(\frac{R_*}{R_\odot}\right)^{\frac{3}{2}} \left(\frac{M_*}{M_\odot}\right)^{-\frac{1}{2}}, \tag{1.9}$$

where both $R_\odot$ and $M_\odot$ are the radius and the mass of the Sun. Should the mass of the black hole be greater or equal to M_{Hills} the passing star gets engulfed rather than tidally stripped or disrupted [Stone, 2015].

It turns out to be useful to introduce the inverse impact factor given as [Stone, 2015]

$$\beta = \frac{R_{\text{tidal}}}{R_{\text{pericenter}}}, \tag{1.10}$$

where $R_{\text{pericenter}}$ stands for the pericentral distance from the black hole. This dependence of the inverse impact factor (1.10) with respect to the system parameters, i.e. the mass of the central body M_{BH}, is plotted in the Figure 1.1.

Let us propose such a set-up where there is a star orbiting around a massive compact object, e.g. a black hole, and we want to describe the change of star's mass $\frac{dM_*}{dt}$ under the assumption that the star enters the area defined by the tidal radius R_{tidal}. In our approximation we will imagine that the star consists of N particles (representing elementary parts of its volume) all having a specific energy e given by the Keplerian formula

$$e = -\frac{Gm}{2a}, \tag{1.11}$$

where m is the mass of a single point-like test particle and a is the semi-major axis of the orbit described by the Kepler third law as

$$a = \left(\frac{t^2 Gm}{4\pi^2}\right)^{\frac{1}{3}}, \tag{1.12}$$

where t is the orbital period. As the stellar body approaches and crosses the tidal radius, it gets damaged and a fraction of its material creates a trail. The remaining trail gradually circularizes and get accreted onto the central body whereas the whole process is governed by the viscous processes. We can write for the accretion rate following relation

$$\frac{dM_*}{dt} = \frac{dM_*}{de}\frac{de}{dt} \approx t^{-\frac{5}{3}}, \tag{1.13}$$

where we took into account that the term $\frac{dM_*}{de}$ is constant and equal to N and $e \approx t^{-\frac{2}{3}}$ which we got after inserting formula (1.12) for a in the equation (1.11). In the first approximation we are presented with the equation (1.13) that is one the five most decisive indicators that we expect from a tidal disruption of a star (or in general, a celestial object). They are as follows (see e.g. [Komossa, 2015] and further references cited therein):

- the bolometric intensity lightcurve decaying as $\approx t^{-\frac{5}{3}}$ (see the equation 1.13),

- the soft X-ray spectra hardening with passing time,

- no activity (of the galactic nucleus) observed prior to the tidal disruption,

- the bolometric luminosities ranging from 10^{45}–10^{46} erg.s^{-1} peaking in the interval of 0.2–2 keV [Montesinos Armijo and de Freitas Pacheco, 2011], with great intensity fluctuations in the spectra compared to those observed in the active galaxies,

- the central body limited by the Hills mass M_{Hills} (see the equation (1.9)).
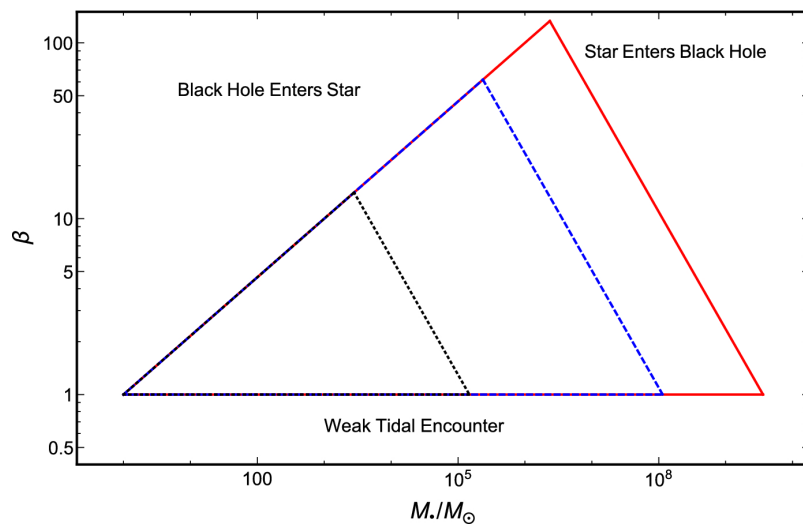
Figure 1.1: Tidal disruption scenarios for *red giants* (red, solid line), *solar-type stars* (blue, dashed line) and *white dwarfs* (black, dotted line). The interpretation of this diagram is as follows – a given type of star can only be disrupted when its parameters lie in its respective triangle, based on the work of [Luminet and Pichon, 1989] focused on the tidal disruption of white dwarfs. For $\beta < 1$ we are presented with not fully disruptive encounters. Stars with parameters in the upper right corner end up swallowed whole by the black hole, as this is described by the black hole's limit mass – the Hills mass given by the equation (1.9), and on the contrary for the upper left corner black hole enters the star. Image credit: [Stone et al., 2019].

1.2 Geometrically thin accretion discs – the surface density equation

Accretion is a process mostly studied in the context of binary stellar systems consisting of a donor and an accretor component. The special case that has been studied are the X-ray binaries with a donor component a Roche lobe overflowing star and a neutron star or black hole as an accretor [Guseinov and Zel'dovich, 1966, Novikov and Zel'dovich, 1966, Shklovsky, 1967], e.g. as in the case of AGN where accretion dumps material onto the surface of a super-massive black hole.

There are different kind of accretion modes, namely spherically symmetric accretion [Bondi, 1952, Hoyle and Lyttleton, 1941] vs. the geometrically thin accretion disc or geometrically thick tori regime. The mass from donor component is, unlike from radially falling onto the accretor's surface in case of spherically symmetric accretion, slowly spiraling onto the surface of accretor creating a disc-like structure called an accretion disc. The gravitational binding energy of the falling material is transformed into kinetic energy and eventually emitted in the form of radiation. It is the viscosity of infalling material that causes it to heat while the gas is transported across the disc.

The basic equation describing the accretion disc is the continuity equation, i.e. the mass conservation equation, complemented by the equations describing conservation of momentum and energy balance [Frank et al., 2002].

In our case we will study the behaviour of systems with a super-massive black hole as the accretor and substitute the donor component for a material that has been tidally stripped off of a passing star. We presume the axial (cylindrical) symmetry of the problem which is a simplification allowing us to proceed with the analytical approaches further albeit the realistic astrophysical regimes are fully described by three-dimensional spatial and temporal dependency.

Let us start with the formulation of the continuity equation. We will do so in the most general way, working with the covariant derivatives

$$\frac{\partial \rho}{\partial t} + (\rho u^{\mu})_{;\mu} = 0, \tag{1.14}$$

where ρ is the density and u^{μ} four-velocity (in our case working in 3 dimensional flat space three-velocity). Since we study the system in Newtonian approximation using curvilinear coordinates R, φ, z let us note that the metric tensor adopts the following form [Zwillinger, 2002]

$$g_{\mu\nu} = \begin{pmatrix} g_{RR} & g_{R\varphi} & g_{Rz} \\ g_{\varphi R} & g_{\varphi\varphi} & g_{\varphi z} \\ g_{zR} & g_{z\varphi} & g_{zz} \end{pmatrix} = \begin{pmatrix} 1 & 0 & 0 \\ 0 & R^2 & 0 \\ 0 & 0 & 1 \end{pmatrix}. \tag{1.15}$$

For the metric tensor given as (1.15) we find only three non-zero components of Christoffel symbols of the first kind

$$\Gamma_{R\varphi\varphi} = -R, \Gamma_{\varphi R\varphi} = \Gamma_{\varphi\varphi R} = R, \tag{1.16}$$

where for their calculation we started from the definition

$$\Gamma_{\eta\mu\nu} = \frac{1}{2}(g_{\eta\mu,\nu} + g_{\eta\nu,\mu} - g_{\mu\nu,\eta}). \tag{1.17}$$

Next, we can rewrite the equation (1.14) as

$$\frac{\partial \rho}{\partial t} + \boxed{\rho_{;\mu}u^{\mu} + \rho u^{\mu}{}_{;\mu}} = 0, \tag{1.18}$$

which taking into account the formula for covariant derivative of any scalar S, any contravariant tensor of the first order A^{μ} and any contravariant tensor of the second order $B^{\mu\nu}$

$$S_{;\nu} = S_{,\nu}, A^{\mu}{}_{;\mu} = A^{\mu}{}_{,\mu} + \Gamma^{\mu}{}_{\sigma\mu}u^{\sigma}, B^{\mu\nu}{}_{;\sigma} = B^{\mu\nu}{}_{,\sigma} + \Gamma^{\mu}{}_{\alpha\sigma}B^{\alpha\nu} + \Gamma^{\nu}{}_{\alpha\sigma}B^{\mu\alpha}, \tag{1.19}$$

can be used for the boxed terms in the equation (1.18) and then leads to

$$\rho_{,\mu}u^\mu + \rho u^\mu{}_{,\mu} + \rho\Gamma^\mu{}_{\sigma\mu}u^\sigma = \rho_{,R}u^R + \rho u^R{}_{,R} + \Gamma^R{}_{\sigma R}u^\sigma + \rho\Gamma^\varphi{}_{\sigma\varphi}u^\sigma + \rho\Gamma^z{}_{\sigma z}u^\sigma$$
$$= \rho_{,R}u^R + \rho u^R{}_{,R} + \rho g^{\varphi\varphi}\Gamma_{\varphi R\varphi}u^R$$
$$= \rho_{,R}u^R + \rho u^R{}_{,R} + \frac{\rho}{R}u^R$$
$$= (\rho u^R R)_{,R}\frac{1}{R}.$$

$$(1.20)$$

As a result of introducing the cylindrical coordinates we get from the general form of (1.14) the continuity equation given as

$$\frac{\partial\rho}{\partial t} + \frac{1}{R}(\rho u^R R)_{,R} = 0,\qquad(1.21)$$

which after the integration in the z-direction ($\int_0^h \rho\,dz = \Sigma$ where Σ denotes the surface density of material in the accretion disc and h the vertical size of the accretion disc) leads to the final form of the continuity equation

$$R\frac{\partial\Sigma}{\partial t} + \frac{\partial}{\partial R}(R\Sigma v_R) = 0.\qquad(1.22)$$

For the derivation of the equation describing the conservation of momentum we start by formulating the Euler equation of motion given as

$$\frac{\partial u^\mu}{\partial t} + u^\nu u^\mu{}_{;\nu} = -\frac{1}{\rho}P_{;}{}^\mu - \Phi_{;}{}^\mu + \frac{1}{\rho}\Pi^{\mu\nu}{}_{;\nu},\qquad(1.23)$$

where $\Pi^{\mu\nu}$ is the stress tensor. We will study the φ-component of the equation (1.23) leading to

$$\frac{\partial u^\varphi}{\partial t} + u^\nu u^\varphi{}_{;\nu} = \frac{1}{\rho}\Pi^{\varphi\nu}{}_{;\nu},\qquad(1.24)$$

not taking into account the pressure and the potential gradient $-\frac{1}{\rho}P_{;}{}^\varphi$ and $-\Phi_{;}{}^\varphi$ terms of the equation (1.23) when setting $\mu = \varphi$. We will work with a special form of stress tensor $\Pi^{\mu\nu}$ given as

$$\Pi^{\mu\nu} = \eta(u^{\mu;\nu} + u^{\nu;\mu} - \frac{2}{3}u^\alpha{}_{;\alpha}\delta^{\mu\nu}),\qquad(1.25)$$

describing its proportionality with four-velocity (in our case three-velocity) using the parameter η called the dynamical viscosity. Now let us work out the second term on the left side of the equation (1.24) looking at the φ-component

$$u^\nu u^\varphi{}_{;\nu} = u^R u^\varphi{}_{;R} + u^\varphi u^\varphi{}_{;\varphi} + u^z u^\varphi{}_{;z}$$
$$= u^R u^\varphi{}_{,R} + u^R\Gamma^\varphi{}_{\varphi R}u^\varphi + u^\varphi u^\varphi{}_{,\varphi} + u^\varphi\Gamma^\varphi{}_{R\varphi}u^R + u^z u^\varphi{}_{,z} + u^z\boxed{\Gamma^\varphi{}_{\alpha z}}u^\alpha$$
$$= u^R u^\varphi{}_{,R} + u^\varphi u^\varphi{}_{,\varphi} + u^z u^\varphi{}_{,z} + 2u^\varphi u^R g^{\varphi\varphi}\Gamma_{\varphi\varphi R}$$
$$= u^R u^\varphi{}_{,R} + u^\varphi u^\varphi{}_{,\varphi} + u^z u^\varphi{}_{,z} + \frac{2}{R}u^\varphi u^R$$
$$= u^R \frac{1}{R^2}\frac{\partial}{\partial R}(R^2 u^\varphi) + \boxed{u^\varphi u^\varphi{}_{,\varphi}} + \boxed{u^z u^\varphi{}_{,z}},$$

$$(1.26)$$

with the boxed terms being equal to zero. Further let us look at the φ-component of covariant divergence of stress tensor in the equation (1.24)

$$
\begin{aligned}
\Pi^{\varphi\nu}{}_{;\nu} &= \Pi^{\varphi\nu}{}_{,\nu} + \Gamma^{\varphi}{}_{\sigma\nu}\Pi^{\sigma\nu} + \Gamma^{\nu}{}_{\sigma\nu}\Pi^{\varphi\sigma} \\
&= \Pi^{\varphi\nu}{}_{,\nu} + g^{\varphi\mu}\Gamma_{\mu\sigma\nu}\Pi^{\sigma\nu} + g^{\nu\mu}\Gamma_{\mu\sigma\nu}\Pi^{\varphi\sigma} \\
&= \Pi^{\varphi R}{}_{,R} + \Pi^{\varphi\varphi}{}_{,\varphi} + \Pi^{\varphi z}{}_{,z} + g^{\varphi\varphi}\Gamma_{\varphi R\varphi}\Pi^{R\varphi} + g^{\varphi\varphi}\Gamma_{\varphi\varphi R}\Pi^{\varphi R} + g^{\varphi\varphi}\Gamma_{\varphi R\varphi}\Pi^{\varphi R} \\
&= \Pi^{\varphi R}{}_{,R} + \Pi^{\varphi\varphi}{}_{,\varphi} + \Pi^{\varphi z}{}_{,z} + \frac{2}{R^2}R\Pi^{\varphi R} + \frac{1}{R^2}R\Pi^{\varphi R} \\
&= \Pi^{\varphi R}{}_{,R} + \Pi^{\varphi\varphi}{}_{,\varphi} + \Pi^{\varphi z}{}_{,z} + \frac{3}{R}\Pi^{\varphi R} \\
&= \boxed{\Pi^{\varphi\varphi}{}_{,\varphi}} + \boxed{\Pi^{\varphi z}{}_{,z}} + \frac{1}{R^3}\frac{\partial}{\partial R}(R^3\Pi^{\varphi R}),
\end{aligned}
\tag{1.27}
$$

with the boxed terms being equal to zero. We are only interested in the third term of the equation (1.27) and using the relation (1.25) we can write

$$
\begin{aligned}
\frac{1}{\eta}\Pi^{\varphi R} &= u^{\varphi;R} + u^{R;\varphi} - \frac{2}{3}u^{\alpha}{}_{;\alpha}\boxed{g^{\varphi R}} \\
&= g^{RR}u^{\varphi}{}_{;R} + g^{\varphi\varphi}u^{R}{}_{;\varphi} \\
&= g^{RR}u^{\varphi}{}_{,R} + g^{RR}g^{\varphi\varphi}\Gamma_{\varphi\varphi R}u^{\varphi} + g^{\varphi\varphi}u^{R}{}_{,\varphi} + g^{\varphi\varphi}g^{RR}\Gamma_{R\varphi\varphi}u^{\varphi} \\
&= u^{\varphi}{}_{,R} + g^{\varphi\varphi}\Gamma_{\varphi\varphi R}u^{\varphi} + \frac{1}{R^2}(u^{R}{}_{,\varphi} + g^{RR}\Gamma_{R\varphi\varphi}u^{\varphi}) \\
&= u^{\varphi}_{R} + \frac{1}{R}u^{\varphi} + \boxed{\frac{1}{R^2}u^{R}{}_{,\varphi}} - \frac{1}{R}u^{\varphi} \\
&= u^{\varphi}{}_{,R},
\end{aligned}
\tag{1.28}
$$

which combining with the result of (1.27), taking into account that terms $\sim \frac{\partial}{\partial\varphi}(...)$ and $\sim \frac{\partial}{\partial z}(...)$ are zero, leads to the formula

$$
\Pi^{\varphi\nu}{}_{;\nu} = \frac{1}{R^3}\frac{\partial}{\partial R}\left(R^3\eta\frac{\partial\Omega}{\partial R}\right),
\tag{1.29}
$$

where we used the fact that $u^{\varphi} = \Omega$. Now we can come back to the equation (1.24) and put in use formulae (1.26) and (1.29)

$$
\frac{\partial u^{\varphi}}{\partial t} + u^{R}\frac{1}{R^2}\frac{\partial}{\partial R}(R^2 u^{\varphi}) = \frac{1}{\rho}\frac{1}{R^3}\frac{\partial}{\partial R}\left(R^3\eta\frac{\partial\Omega}{\partial R}\right).
\tag{1.30}
$$

Taking the respective derivatives of (1.30) and multiplying by ρR

$$
R\rho\frac{\partial u^{\varphi}}{\partial t} + Ru^{\varphi}\frac{\partial\rho}{\partial t} + \frac{1}{R^2}(R\rho u^{R})\frac{\partial}{\partial R}(R^2 u^{\varphi}) + \frac{1}{R}(Ru^{\varphi})\frac{\partial}{\partial R}(R\rho U^{R}) = \\
= \frac{1}{R^2}\left(R^3\eta\frac{\partial\Omega}{\partial R}\right),
\tag{1.31}
$$

which after multiplying the whole equation by R^2 and re-arranging the terms leads to

$$
R^3\left(\rho\frac{\partial u^{\varphi}}{\partial t} + u^{\varphi}\frac{\rho}{\partial t}\right) + \frac{\partial}{\partial R}(R^3\rho u^{R}u^{\varphi}) = \frac{\partial}{\partial R}\left(R^3\eta\frac{\partial\Omega}{\partial R}\right)
\tag{1.32}
$$

further rewritten as

$$R^3 \frac{\rho u^\varphi}{\partial t} + \frac{\partial}{\partial R}(R^3 u^R u^\varphi \rho) = \frac{\partial}{\partial R}\left(R^3 \nu \rho \frac{\partial \Omega}{\partial R}\right), \tag{1.33}$$

where we used the fact that the dynamic viscosity η relates to the kinematic viscosity ν via relation $\eta = \rho\nu$. Taking into account that $u^\varphi = \Omega$ (angular velocity), $u_R = v_R$ (radial velocity) and $v_\varphi = R\Omega$ we can after the integration in the z-direction ($\int_0^h \rho\, dz = \Sigma$) write the equation (1.33) in the following form

$$R\frac{\partial(\Sigma R v_\varphi)}{\partial t} + \frac{\partial}{\partial R}(R^2 v_R v_\varphi \Sigma) = \frac{\partial}{\partial R}\left(R^3 \nu \Sigma \frac{\partial \Omega}{\partial R}\right), \tag{1.34}$$

usually written as

$$R\frac{\partial}{\partial t}(R\Sigma v_\varphi) + \frac{\partial}{\partial R}(R^2 \Sigma v_R v_\varphi) = \frac{1}{2\pi}\frac{\partial G}{\partial R}, \tag{1.35}$$

where G is R-dependent quantity called the gravitational torque, describing the angular momentum transfer between radii, defined as [Frank et al., 2002]

$$G(R) = 2\pi\nu\Sigma R^3 \frac{d\Omega}{dR}. \tag{1.36}$$

Both of the equations (1.22) and (1.35) were obtained assuming their most general forms by accepting the axial symmetry $\frac{\partial}{\partial\varphi} = 0$ and further assumptions like $v_\varphi \gg v_R \gg v_z$ of the studied problem. We can modify the equation (1.35) into

$$\boxed{R^2 v_\varphi \frac{\partial \Sigma}{\partial t}} + R\Sigma\frac{\partial}{\partial t}(v_\varphi R) + \boxed{R v_\varphi \frac{\partial}{\partial R}(R\Sigma v_R)} + R\Sigma v_R\frac{\partial}{\partial R}(R v_\varphi) = \frac{1}{2\pi}\frac{\partial G}{\partial R} \tag{1.37}$$

and noticing that the boxed terms gives us the continuity equation (1.22) and after we isolate Rv_φ we get 0. Moreover the second term of the equation (1.37) is also 0 because both R and v_φ are independent variables. Therefore we are left with

$$R\Sigma v_R \frac{\partial}{\partial R}(R v_\varphi) = \frac{1}{2\pi}\frac{\partial G}{\partial R}. \tag{1.38}$$

Now we assume the angular velocity having the Keplerian value given as

$$\Omega = \Omega_{\text{Kepler}} = \left(\frac{GM}{R^3}\right)^{\frac{1}{2}}. \tag{1.39}$$

At the end we get the heat equation-like partial differential equation

$$\frac{\partial \Sigma}{\partial t} = \frac{3}{R}\frac{\partial}{\partial R}\left[R^{\frac{1}{2}}\frac{\partial}{\partial R}(\nu\Sigma R)\right], \tag{1.40}$$

working with the continuity equation (1.22) and following relations

$$\frac{d\Omega}{dR} = -\frac{3}{2}\left(\frac{GM}{R^5}\right)^{\frac{1}{2}}, \frac{d(\Omega R^2)}{dR} = \frac{(GM)^{\frac{1}{2}}}{2R^{\frac{1}{2}}}, G(R) = -3\pi\nu\Sigma(GMR)^{\frac{1}{2}}. \tag{1.41}$$

11

Given the appropriate substitution and taking into account that we want the kinematic viscosity η to be constant we can rewrite the formula (1.40) as

$$\frac{\partial \Sigma R^{\frac{1}{2}}}{\partial t} = \frac{12\nu}{x^2} \frac{\partial^2}{\partial x^2}(\Sigma R^{\frac{1}{2}}), \qquad (1.42)$$

where we used following

$$x = 2R^{\frac{1}{2}}, \frac{\partial}{\partial R} = \frac{2}{x} \frac{\partial}{\partial x}. \qquad (1.43)$$

Let us substitute $\Sigma R^{\frac{1}{2}}$ with U and rewrite the equation (1.42) to

$$\frac{\partial U}{\partial t} = \frac{12\nu}{x^2} \frac{\partial^2 U}{\partial x^2}. \qquad (1.44)$$

Taking into account the initial mass ring surface density profile in the form of delta-distribution at the radius $R = R_0$ we write

$$\Sigma(R, t = 0) = \frac{m}{2\pi R_0} \delta(R - R_0). \qquad (1.45)$$

The solution to the equation (1.42) with respect to the initial condition given as (1.45) and boundary conditions $\Sigma(R_{\text{inner}} = 0, t) = \Sigma(R_{\text{outer}}, t) = 0$ can be analytically written as [Frank et al., 2002]

$$\Sigma(x, \tau) = \frac{m}{\pi R_0^2} \tau^{-1} x^{-\frac{1}{4}} \exp\left\{ -\frac{(1 + x^2)}{\tau} \right\} I_{\frac{1}{4}}\left(\frac{2x}{\tau}\right), \qquad (1.46)$$

where

$$x = \frac{R}{R_0}, \tau = 12\nu t R_0^{-2} \qquad (1.47)$$

are both dimensionless quantities and $I_{\frac{1}{4}}$ is the modified Bessel function.

The Figure 1.2 depicts the analytical solution for the diffusion equation given by the equation (1.46) for a chosen set of parameters τ.
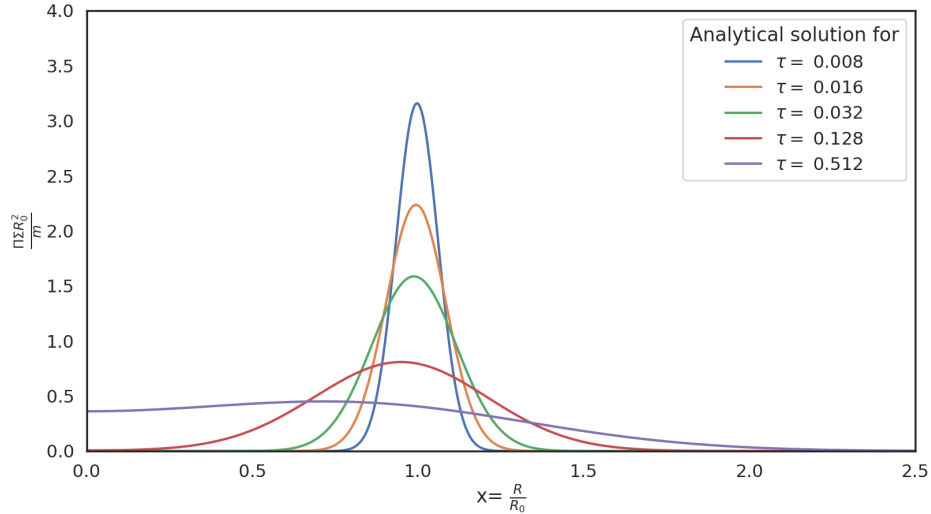
Figure 1.2: Analytical solution to the diffusion equation (1.40) describing the evolution of the surface density profile of the initial mass ring located at R_0.

Once we set the $\frac{\partial}{\partial t} = 0$ the conservation equations (1.22) and (1.35) simplify to

$$\frac{\partial R\Sigma v_R}{\partial R} = 0 \tag{1.48}$$

and

$$\frac{\partial}{\partial R}(R^2\Sigma v_R v_\varphi) = \frac{1}{2\pi}\frac{\partial G}{\partial R}. \tag{1.49}$$

We define, based on the equation (1.48), the mass accretion rate as [Frank et al., 2002]

$$\dot{M} = -2\pi\Sigma v_R \tag{1.50}$$

with the minus sign since $v_R < 1$ and the equation (1.49), taking into account the equation (1.50) and (1.36), as [Frank et al., 2002]

$$\nu\Sigma = \frac{\dot{M}}{3\pi}\left[1 - \left(\frac{R_{\text{inner}}}{R}\right)^{\frac{1}{2}}\right]. \tag{1.51}$$

Setting Ω to Ω_{Kepler} as in the equation (1.39) we can define the viscous energy dissipation rate per unit are of the accretion disc as follows [Frank et al., 2002]

$$D(R) = \frac{3GM\dot{(M)}}{8\pi R^3}\left[1 - \left(\frac{R_{\text{inner}}}{R}\right)^{\frac{1}{2}}\right]. \tag{1.52}$$

To calculate the infinitesimal luminosity contribution generated by the accretion disc between the radii R_{inner} and R_{outer} we write [Frank et al., 2002]

$$L_{\text{disc}}(R_{\text{inner}}, R_{\text{outer}}) = s\int_{R_{\text{inner}}}^{R_{\text{outer}}} D(R)\pi RdR, \tag{1.53}$$

which can be taking by the limit of $R_{\text{outer}} \to \infty$ rewritten as [Frank et al., 2002]

$$L_{\text{disc}} = \frac{GM\dot{M}}{R_{\text{inner}}} = \frac{1}{2}L_{\text{acc}}, \tag{1.54}$$

where L_{acc} is the accretion luminosity. The equation describing the radial temperature profile of the accretion disc follows the formula [Frank et al., 2002]

$$T(R) = \left\{\frac{3GM\dot{M}}{8\pi R^3\sigma}\left[1 - \left(\frac{R_{\text{inner}}}{R}\right)^{\frac{1}{2}}\right]\right\}^{\frac{1}{4}}, \tag{1.55}$$

where $\dot{M}$ is the accretion rate constant, σ the Stefan-Boltzmann constant and R_{inner} is the inner radius of the accretion disc (located on the surface of the central body or the last stable circular orbit, etc.). If H is the typical scaleheight in the z-direction we can write

$$H = \frac{c_{\text{s}}}{\sqrt{GM}}R^{\frac{3}{2}}, \tag{1.56}$$

whereby the thin disc assumption $\frac{H}{R} \ll 1$ leads to

$$c_{\text{s}} \ll \left(\frac{GM}{R}\right)^{\frac{1}{2}} = \Omega_{\text{Kepler}}R = v_{\text{Kepler}}, \tag{1.57}$$

i.e. the Keplerian velocity v_{Kepler} must be higher than the speed of sound c_{c} (supersonic) [Frank et al., 2002].

1.2.1 Shakura-Sunyaev standard accretion disc model

The following key points summarize the standard Shakura-Sunyaev accretion disc model [Shapiro and Teukolsky, 1983]

- the contribution of the accretion disc to the gravitational field is neglected, i.e. the gravitational field is generated only by the central body,

- the accretion disc is assumed to be steady,

- the accretion disc is assumed to be axially symmetric,

- the accretion disc is assumed to be thin, i.e. $\frac{H}{R} \ll 1$,

- the radial inflow velocity is neglected, i.e. $\frac{v_R}{v_\varphi} \ll 1$,

- the accretion disc is assumed to be in hydrostatic equilibrium and optically thick in the vertical direction.

The kinematic viscosity ν is defined as follows [Frank et al., 2002]

$$\nu = \alpha c_{\mathrm{s}} H, \tag{1.58}$$

where α is a parameter of so-called standard model describing the Shakura-Sunyaev accretion disc structure. In order to obtain physically reasonable solutions the semi-empirical α prescription must obey the inequality $\alpha \lesssim 1$.

The viscous, also noted as drift or diffusion timescale describes the time horizon over which the accretion disc's surface density profile changes and is given by the equation [Frank et al., 2002]

$$t_{\mathrm{viscous}} \approx \frac{R^2}{\nu}. \tag{1.59}$$

The dynamical timescale $t_{\mathrm{dynamical}}$ describing the time of azimuthal motion of accretion disc's rotating material. Both the viscous and dynamical timescale relate to each other as [Frank et al., 2002]

$$t_{\mathrm{viscous}} \gg t_{\mathrm{dynamical}} = \frac{r}{v_\varphi} = \frac{1}{\Omega}, \tag{1.60}$$

where Ω is the Keplerian angular velocity given by the equation (1.77). The changes in the vertical direction of the accretion disc are balanced out over the hydrodynamical timescale $t_{\mathrm{hydrodynamical}}$ related to the viscous timescale by the formula [Frank et al., 2002]

$$t_{\mathrm{viscous}} \gg t_{\mathrm{hydrodynamical}} = \frac{H}{c_{\mathrm{s}}}. \tag{1.61}$$

Similar inequality holds for the thermal timescale t_{thermal} describing the temperature profile re-adjustment back to the thermal equilibrium across the whole accretion disc [Frank et al., 2002]

$$t_{\mathrm{viscous}} \gg t_{\mathrm{thermal}}. \tag{1.62}$$

1.3 Relativistic effects in spectral lines from gaseous rings and accretion discs

Based on the activity the galactic cores can be distinguished as active and inactive ones. The active galactic nuclei or AGN are supposed to have a super-massive black hole at its centre surrounded by the accretion disc (see [Kazanas et al., 2012] and the references therein). The amount of radiation produced by inactive galaxies is incomparable to that of active ones. They are however also suspected to have a super-massive black hole at its centre. Such quiescent galaxies quietly lurking in the universe are perfect targets to study of tidal disruption using the observation of sudden brightening in their spectra.

The mass accretion onto a central body, e.g. a stellar-mass black hole, an intermediate black hole or a super-massive one that is believed to be in the centre of every galaxy [Magorrian et al., 1998], is accompanied by a high temperature material falling in on it. The reason for such high temperatures lies within the friction forces that the material's constituents act upon each other and ultimately invoke the emission of electromagnetic radiation. The electromagnetic radiation coming from the galactic nuclei spans across all bands with the major contribution in the X-ray and UV spectra. In order to to pursue the observations of the galactic cores in the optical one must wait for the density profile of the circum-nuclear material to drop. Only then it will be possible to observe the radiation that is a result of the reprocessed initial thermal radiation.

The radiation coming from central parts of galactic centre is strongly affected by the gravity of its central body. One can study the properties of the observed radiation (e.g. the radiation profile) taking different approximations. In the classical view the radiation gets only Doppler shifted. In the special relativistic case with the velocities close to the speed of light we end up with more general form of Doppler shift a special case called the Doppler transverse redshift. The general relativity adds in the object's mass influence on the trajectory of light – an effect called the light bending. Both the special relativistic and the general relativistic approach cause the peaks of the spectra to be asymmetric meaning the blueshifted peak is higher than the redshifted one which is a direct consequence of the Liouville's theorem.

The Fe Kα emission line forms a prominent energy excess at around 6.4 keV. It is found in the X-ray spectra of some AGNs (e.g. [Liu et al., 2017] and references therein) whereas it is also the strongest one observed. Physical mechanism behind the origin of line with such a magnitude lies within the interaction of high energy photons coming from the surrounding corona and the accretion disc's plasma spiraling down to the surface of the central body. Hard X-ray radiation emission will accompany the jump of the excited electron from the energy level n=2 back to the energy level n=1 in case of the Kα emission line. For the Kβ line the electron jump occurs from energy level n=3 to energy level n=1. It is due to strength of that particular emission line caused by its origin in close proximity of super-massive black hole that enables us to study the effects of general relativity. The first FeKα line was observed by [Tanaka et al., 1995] (see Figure 3) and studied by [Fabian et al., 1989a, Kojima, 1991]. Over the years of the continuous study of X-ray radiation coming from numerous AGN there we developed models to fit the energy excess found in the spectra based on the data from the observations done

by Chandra, Swift, XMM Newton, etc. It is the XSPEC `laor` model component [Laor, 1991] and `kyrline` model component [Dovčiak et al., 2004] that are used to model the spectral line profiles in case of taking into account the zero or non-zero angular momentum of the central object. The article by [Kara et al., 2016] proposed that the energy excess resembling that of an iron emission spectral line may possibly be also found in the early stages of a tidal disruption.

What we will focus on is the time evolution of a spectral line emitted from an accretion disc due to the interaction of high energy photons of corona with it. We assume the initial mass ring to be created as a result of the tidal disruption of a celestial object (a star) and evolving in time into an accretion disc as schematically depicted by Figure 1.3 with the corona present throughout the whole process.
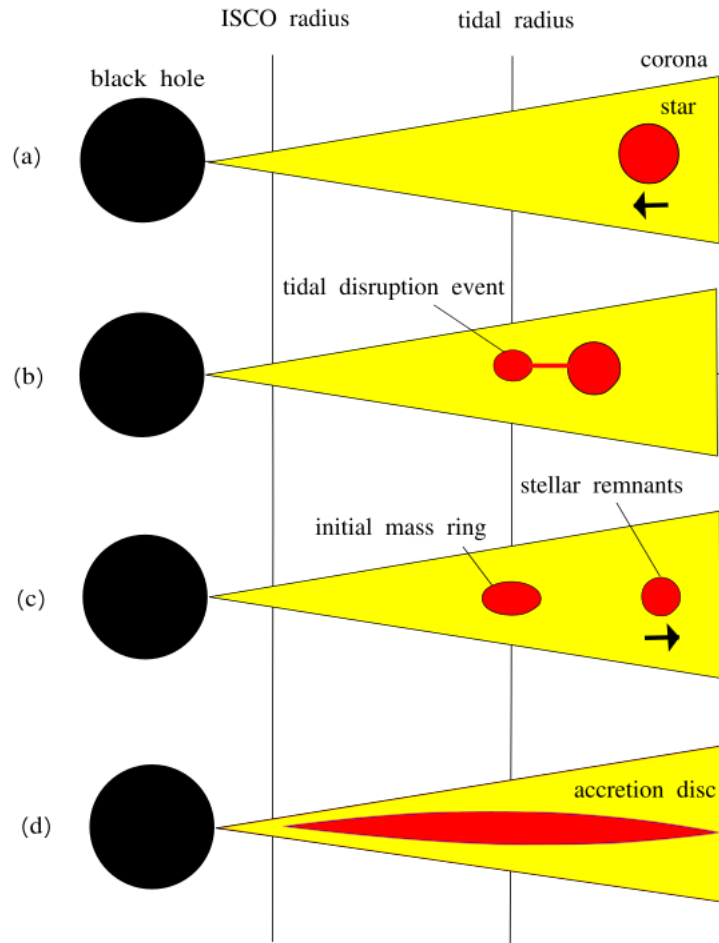
Figure 1.3: Vertical cross section through the galactic centre involving a black hole as its central object, a star and a corona as a high-energetic interactive medium surrounding the galactic centre: (a) the star approaching the central object of the galactic centre - the black hole, (b) the tidal disruption event involving mass transfer as the star gets closer to the tidal radius given by the equation (1.7), (c) the initial mass ring (at time $t = 0$) and the stellar remnants flying away, (d) the accretion disc as a results of the diffusion equation given by the equation (1.40) (at time $t \neq 0$).

1.3.1   Liouville's theorem and intensity-frequency formula

Let us calculate the infinitesimal phase-space volume element dV for the phase-space (x, p_x) and dV' for (x', p'_x)

$$dV = dx\,dp_x, \quad dV' = dx'\,dp'_x. \tag{1.63}$$

Further rewriting the dx' and dp'_x using the special relativistic Lorentz transformation as follows

$$dx = \sqrt{1 - \frac{v^2}{c^2}}\,dx' \text{ (length contraction)},$$

$$dp_x = \frac{dp'_x}{\sqrt{1 - \frac{v^2}{c^2}}} \text{ (momentum transformation relation)}, \tag{1.64}$$

which leads to a conclusion that

$$dV = dx\,dp_x = \sqrt{1 - \frac{v^2}{c^2}}\,dx' \frac{dp'_x}{\sqrt{1 - \frac{v^2}{c^2}}} = dx'\,dp'_x = dV',$$

$$dV = \text{Lorentz invariant}. \tag{1.65}$$

With the help of the Liouville's theorem in the form of the equation (1.65) we write for the volume V of phase-space (x, y, z, p_x, p_y, p_z) following

$$\text{Lorentz invariant} = V = V_{\text{space}} V_{\text{momenta}} = c\,dt\,dS\,p^2\,dp\,d\Omega. \tag{1.66}$$

Given the fact that photon momentum can be expressed as

$$p = \frac{h\nu}{c} \tag{1.67}$$

and putting it in use in the equation (1.66) we see that, the Planck constant h and the speed of light c being both constants, $dt\,dS\,\nu^2\,d\nu\,d\Omega$ is constant and using the formulae for the infinitesimal energy element of the radiation dE

$$dE = I_\nu\,dt\,dS\,d\nu\,d\Omega, \quad dE = h\nu dN \tag{1.68}$$

we can study the following specific combination of specific intensity I_ν and frequency ν

$$\frac{I_\nu}{\nu^3} = \frac{dE}{\nu^3\,dt\,dS\,d\nu\,d\Omega} = \frac{h\nu dN}{\nu\,dt\,dS\,\nu^2\,d\nu\,d\Omega} = \text{constant}. \tag{1.69}$$

Therefore we can write

$$\frac{I_{\text{observed}}}{I_{\text{emitted}}} = \frac{\nu^3_{\text{observed}}}{\nu^3_{\text{emitted}}} = \text{constant}. \tag{1.70}$$

where I_{observed}, I_{emitted}, ν_{observed} and ν_{emitted} are the observed and the emitted values of intensity and frequency respectively.

1.3.2 Redshift factor in Newtonian, special relativistic and general relativistic scenario

We define the redshift factor as

$$g = \frac{\nu_{\text{observed}}}{\nu_{\text{emitted}}}.$$ (1.71)

Let S′ be the rest-frame of the radiation source whereas S will be the observer's rest-frame. We choose the S′ frame to be located so that it moves with a velocity v in the positive direction of x-axis. We define the wave four-vector k^μ and k'^μ as follows

$$k^\mu = \frac{\omega}{c}(1, \cos(\varphi)\sin(I), \sin(\varphi)\sin(I), cos(I)),$$
$$k'^\mu = \frac{\omega'}{c}(1, \cos(\varphi')\sin(I'), \sin(\varphi')\sin(I'), cos(I')),$$ (1.72)

where φ and φ' denote the azimuthal variables and I and I' the inclination of the radiation source in S and S' respectively. The Figure 1.4 depicts our interpretation of the variable set-up in the observer's rest-frame S in context of the radiation from the accretion disc.

The wave four-vectors k'^μ and k^μ are bound by the special relativistic Lorentz transformation expressed as

$$k'^\mu = \Lambda^\mu{}_\nu k^\nu$$ (1.73)

with the special relativistic Lorentz transformation matrix $\Lambda^\mu{}_\nu$ taking into account the motion in the positive direction of x axis and represented as

$$\Lambda^\mu{}_\nu = \begin{pmatrix} \gamma & -\gamma\beta & 0 & 0 \\ -\gamma\beta & \gamma & 0 & 0 \\ 0 & 0 & 1 & 0 \\ 0 & 0 & 0 & 1 \end{pmatrix}.$$ (1.74)

Following the rules of Einstein summation we write the equation (1.73) as

$$k'^0 = \frac{\omega'}{c} = \Lambda^0{}_0 k^0 + \Lambda^0{}_i k^i = \gamma\frac{\omega}{c} - \gamma\beta\frac{\omega}{c}\cos(\varphi)\sin(I).$$ (1.75)

Using the formula $\omega = 2\pi\nu$ we rewrite the equation (1.75) in context of our definition of the redshift factor (1.71) as

$$\frac{\omega_{\text{observed}}}{\omega_{\text{emitted}}} = \frac{\nu_{\text{observed}}}{\nu_{\text{emitted}}} = g_{\text{STR}}(R, \varphi, I) = \frac{1}{\gamma(1 - \frac{v\cos(\varphi)\sin(I)}{c})},$$ (1.76)

where velocity v is the velocity of Keplerian rotation defined as

$$v = v_{\text{Kepler}} = \sqrt{\frac{GM_{\text{BH}}}{R}},$$ (1.77)

which multiplied by $\cos(\varphi)\sin(I)$ is equal to the radial velocity shifted in the line of sight of the observer located in the infinity. In case we study the velocities for

which $v \ll c$ the relativistic gamma factor behaves as $\gamma \to 1$ and the equation (1.76) can be written as

$$g_{\text{NEWTONIAN}}(R, \varphi, I) = \frac{1}{1 - \frac{v \cos(\varphi) \sin(I)}{c}}. \tag{1.78}$$

Comparing the equation (1.76) and (1.78) one can observe that there is a non-zero redshift factor possibility even though the radial velocity is equal to zero. This type of redshift occurs for φ values $\frac{\pi}{2}$ and $\frac{3\pi}{2}$ called the special relativistic transverse Doppler shift given as

$$g_{\text{STR}-\text{TRANSVERSE}}(R) = \frac{1}{\gamma}. \tag{1.79}$$

As mentioned above (see section 1.1) the tidal disruption scenario favors a set-up in which the accretor component is a massive compact object, e.g. a super-massive black hole. According to the No-hair theorem black holes can be described by three parameters - mass M_{BH}, charge Q and angular momentum (spin) a [Misner et al., 1973]. The space-time metric around a rotating charged point mass can be described by the Kerr-Newman metric [Newman et al., 1965]. When setting the charge Q to 0 the Kerr-Newman metric simplifies to the Kerr metric generated by a rotating point mass [Kerr, 1963]. Setting the angular momentum a to 0 results in the Reissner-Nordström solution [Nordström, 1918, Reissner, 1916] and further setting the charge Q to 0 leads to the Schwarzschild solution. The Schwarzschild, the spherically symmetric, static, vacuum solution, solution for a non-rotating mass with zero charge, is given as

$$ds^2 = -\left(1 - \frac{2}{R}\right)dt^2 + \frac{1}{(1 - \frac{2}{R})}dR^2 + R^2 d\Omega^2 \tag{1.80}$$

with geometrized units G and c both set to 1, R measured in units of M and $d\Omega^2 = d\theta^2 + \sin^2(\theta)d\varphi^2$ ($\theta \in [0, \pi]$ and $\varphi \in [0, 2\pi]$). Whereas the special relativistic form of the redshift factor (1.76) describes the radiation behaviour when reaching the velocities close to the speed of light the general relativistic redshift factor formula takes into account also the light bending. To express the redshift for a set-up with a non-rotating black hole with no charge we will make use of the general relativistic redshift factor formula [Pecháček et al., 2005]

$$g(R, \varphi, I)_{\text{GTR}} = \frac{\sqrt{R(R - 3)}}{R + \sin(\varphi)\sin(I)\sqrt{R - 2 + 4(1 + \cos(\varphi)\sin(I))^{-1}}}. \tag{1.81}$$
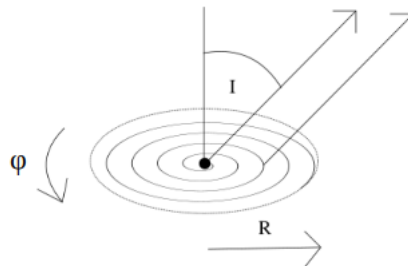
Figure 1.4: Radial variable R, azimuthal variable φ and inclination of the radiation source I in the observer's rest-frame S.

2. Results

2.1 Numerical solution of surface density equation

The inherent idea about the numerical solution to the equation (1.42) lies within the solution of the equation (1.44). Let us split the spatial and temporal dimensions, limited by $t_{\max}$ and $x_{\max}$ into infinitesimal elements Δx and Δt respectively as

$$\Delta x = \frac{x_{\max}}{n_x - 1}, \Delta t = \frac{t_{\max}}{n_t - 1}. \tag{2.1}$$

where n_x and n_t are denote the total number of spatial and temporal nodes of the created grids. For U in point $x_i + \Delta x$ holds

$$U(x_i + \Delta x) = U(x_i) + \Delta x \frac{\partial U}{\partial x}\Big|_{x=x_i} + \frac{\Delta x^2}{2!} \frac{\partial^2 U}{\partial x^2}\Big|_{x=x_i} + \frac{\Delta x^3}{3!} \frac{\partial^3 U}{\partial x^3}\Big|_{x=x_i} + ... \tag{2.2}$$

For U in point $x_i - \Delta x$ holds

$$U(x_i - \Delta x) = U(x_i) - \Delta x \frac{\partial U}{\partial x}\Big|_{x=x_i} + \frac{\Delta x^2}{2!} \frac{\partial^2 U}{\partial x^2}\Big|_{x=x_i} - \frac{\Delta x^3}{3!} \frac{\partial^3 U}{\partial x^3}\Big|_{x=x_i} + ... \tag{2.3}$$

Our notation will be $U(x_i + \Delta x) = U_{i+1}$, $U(x_i) = U_i$ and $U(x_i - \Delta x) = U_{i-1}$. Using the equations (2.2) and (2.3) for U_{i+1}, U_i and U_{i-1} we get the forward and backward spatial difference

$$\frac{U_{i+1} - U_i}{\Delta x} + o(\Delta x) = \frac{\partial U}{\partial x}\Big|_{x=x_i}, \frac{U_i - U_{i-1}}{\Delta x} + o(\Delta x) = \frac{\partial U}{\partial x}\Big|_{x=x_i}, \tag{2.4}$$

which can be rewritten as

$$\begin{aligned} U_{i+1} &= U_i + \Delta x \frac{\partial U}{\partial x}\Big|_{x=x_i} + \frac{\Delta x^2}{2!} \frac{\partial^2 U}{\partial^2 x}\Big|_{x=x_i} + ..., \\ U_{i-1} &= U_i - \Delta x \frac{\partial U}{\partial x}\Big|_{x=x_i} + \frac{\Delta x^2}{2!} \frac{\partial^2 U}{\partial^2 x}\Big|_{x=x_i} - ... \end{aligned} \tag{2.5}$$

Now let us combine the equations (2.5) by subtracting one from another and we get

$$U_{i+1} - U_{i-1} = 2\Delta x \frac{\partial U}{\partial x}\Big|_{x=x_i} + o(\Delta x^3) + ..., \tag{2.6}$$

which is usually called the central difference formula of the first order. After combining the equations (2.5) and summing them up

$$U_{i+1} + U_{i-1} = 2U_i + \Delta x^2 \frac{\partial^2 U}{\partial x^2}\Big|_{x=x_i} + o(\Delta x^4) + ..., \tag{2.7}$$

which after rearranging leads to

$$\frac{\partial^2 U}{\partial x^2}\Big|_{x=x_i} = \frac{U_{i+1} - 2U_i + U_{i-1}}{\Delta x^2} + o(\Delta x^2), \tag{2.8}$$

we get what is called the central difference formula of the second order. By analogy with the equations (2.4) we can write for the temporal part of the equation

$$\frac{\partial U}{\partial t}\bigg|_{x=x_i} = \frac{U_i^{m+1} - U_i^m}{\Delta t} + (\Delta t). \tag{2.9}$$

Now when we rewrite the equation (1.44) using the equations (2.8) and (2.9) we get

$$\frac{U_i^{m+1} - U_i^m}{\Delta t} + o(\Delta t) = \frac{12\nu}{x_i^2} \frac{U_{i+1}^m - 2U_i^m + U_{i-1}^m}{\Delta x^2} + o(\Delta x^2). \tag{2.10}$$

We can rewrite the equation (2.10) in a more straight forward way (see [Bath and Pringle, 1981])

$$U_i^{m+1} = \frac{12\nu\Delta t}{x_i^2 \Delta x^2}(U_{i+1}^m + U_{i-1}^m - 2U_i^m) + U_i^m \tag{2.11}$$

with the truncation errors $o(\Delta t)$ and $o(\Delta x^2)$ in temporal and spatial direction respectively.

In order to satisfy the equation (2.11) in terms of obtaining a numerically stable solution there is a certain condition has to be met called von Neumann stability criterion. In this case it can be expressed as (see [Bath and Pringle, 1981])

$$\frac{12\nu\Delta t}{x_i^2 \Delta x^2} < \frac{1}{2}. \tag{2.12}$$

2.2 Initial assumptions and the resulting surface density profile

With help of speed of sound c_{s} in form

$$c_{\mathrm{s}}^2 = \frac{k_{\mathrm{b}}T}{\mu m_{\mathrm{p}}}, \tag{2.13}$$

where k_{b} is the Boltzmann constant, μ the mean molecular mass and m_{p} the mass of a proton, and the formula describing the typical scaleheight H (1.56), we can rewrite the equation (1.58) to get an approximate order of the value of the kinematic viscosity as

$$\nu = \frac{\alpha k_{\mathrm{b}}T}{\mu\sqrt{GM}}R^{\frac{3}{2}}. \tag{2.14}$$

As we aim to study the system spatial evolution on the scale of gravitational radii we want to express the kinematic viscosity in appropriate dimension $\frac{R_{\mathrm{g}}^2}{s}$ instead of $\frac{m^2}{s}$ the equation (2.14) converts to

$$\nu = \frac{\alpha k_{\mathrm{b}}T}{\mu m_{\mathrm{p}}\sqrt{GM}} \frac{1}{R_{\mathrm{g}}^{\frac{1}{2}}} n^{\frac{3}{2}} = C_\nu n^{\frac{3}{2}}, \tag{2.15}$$

with $R = nR_{\mathrm{g}}$. The constant C_ν provides the sought approximate order of the value of the kinematic viscosity. However it depends on the mass of the central object and the black-body temperature at which the initial mass ring and the

accretion disc afterwards radiates. To get the order of temperature we use the equation describing the radial temperature profile of the accretion disc (1.55) and the equation (1.54), limited by the Eddington luminosity of a star with mass M_*, that is being accreted, given as [Frank et al., 2002]

$$L_{\text{Edd}} = \frac{4\pi G M_* m_p c}{\sigma_{\text{T}}} \cong 1.3 \times 10^{38} \frac{M_*}{M_\odot} \text{erg.s}^{-1} = 1.3 \times 10^{31} \frac{\text{M}_*}{\text{M}_\odot} \text{W}, \qquad (2.16)$$

where m_{p} is the mass of a proton and σ_{T} is the Thompson scattering cross section.

Refraining from direct usage of delta distribution as an initial condition in our numerical simulations we rather used the analytical solution itself in a "close to zero" time $\tau = 0.008$ across the whole thesis. In sense of von Neumann stability criterion (2.12) we obtained the results for the numerical integration of the equation (1.40) with its analytical solution (1.46) using the same boundary conditions, i.e. $\Sigma(R_{\text{inner}} = 0, t) = \Sigma(R_{\text{outer}}, t) = 0$. In this case the accretion disc is supposed to extend to the surface of the central object. Given the fact that the equation (1.40) describes the surface density profile in Newtonian approximation we need to re-define the boundary conditions in such a way that the surface density profile will be cut off and set to zero at the innermost stable circular orbit (ISCO) radius R_{ISCO}. Assuming a slowly rotating or non-rotating central super-massive black hole, described by the Schwarzschild solution, the value of the ISCO radius R_{ISCO} will be $6R_g = 3R_S$, as $R_S = 2R_g$ where R_g is defined by the equation (1.8). The boundary conditions for such a set-up will therefore be $\Sigma(R_{\text{ISCO}} = 6R_g, t) = \Sigma(R_{\text{outer}}, t) = 0$.

The Figure 2.1 shows the results of our numerical integration for the equation (1.46) in a sense that we compared the $1\% - 5\%$ multiple of analytical solution with the difference of numerical and analytical solution, both with boundary conditions $\Sigma(R_{\text{inner}} = 0, t) = \Sigma(R_{\text{outer}}, t) = 0$. The following Figures 2.2 to 2.5 show the error of our numerical solution compared to the analytical one for a given time respectively. We can see that the accuracy of numerical solution grows as grows the dimensionless time-resembling parameter τ. We have also investigated as to where the mass median of the ring in a given time extends given different boundary conditions $\Sigma(R_{\text{inner}} = 0, t) = \Sigma(R_{\text{outer}}, t) = 0$ and $\Sigma(R_{\text{ISCO}} = 6R_g, t) = \Sigma(R_{\text{outer}}, t) = 0$ of the studied system (see Figure 2.6 and 2.7). As expected the mass median position nears that of the central body but varies for larger timescales as depicted by the Figure 2.8.
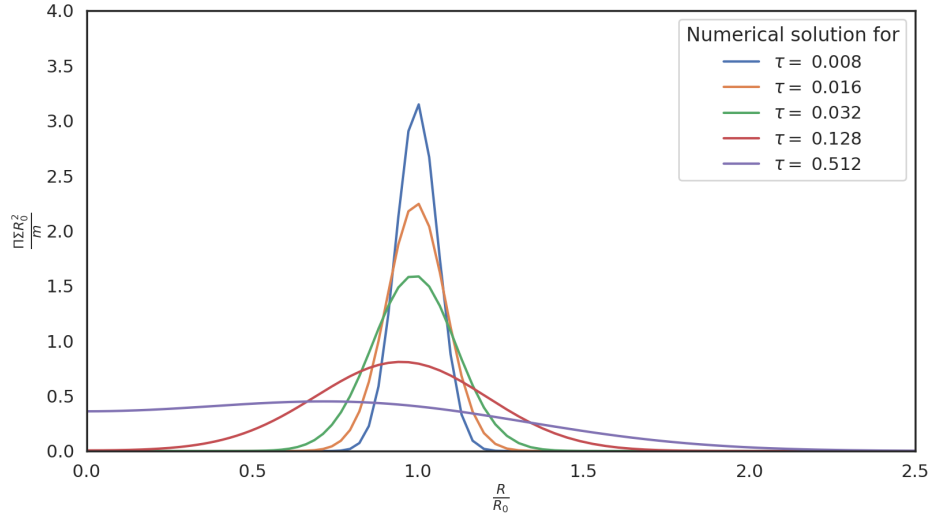
Figure 2.1: Numerical solution to the diffusion equation (1.40) describing the evolution of the surface density profile of the initial mass ring located at $R_0 = 23.6 R_\mathrm{g}$.
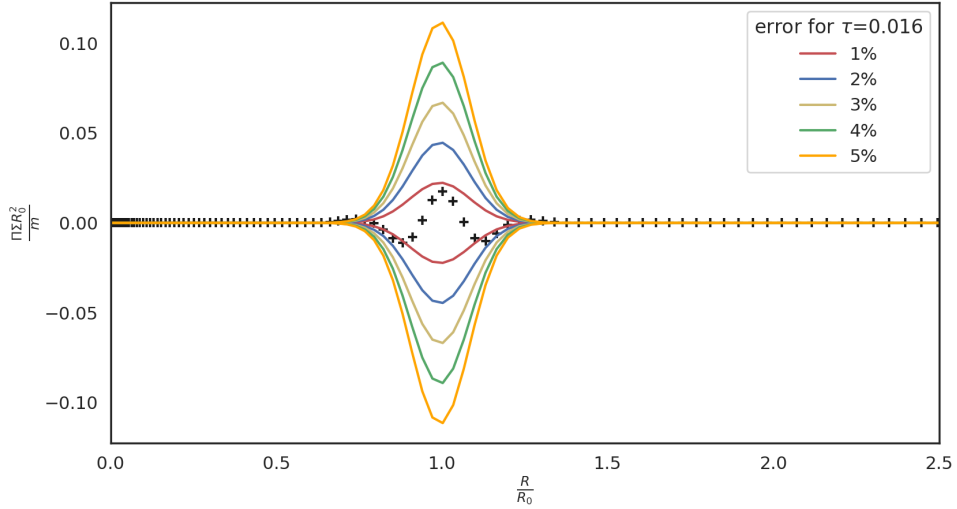
Figure 2.2: Errors of the numerical solution in comparison to analytical solution for $\tau = 0.016$ with the initial mass ring located at $R_0 = 23.6 R_\mathrm{g}$. The errors marked by black crosses and evaluated relative to the $1\% - 5\%$ multiple of the absolute value of the coresponding surface density.
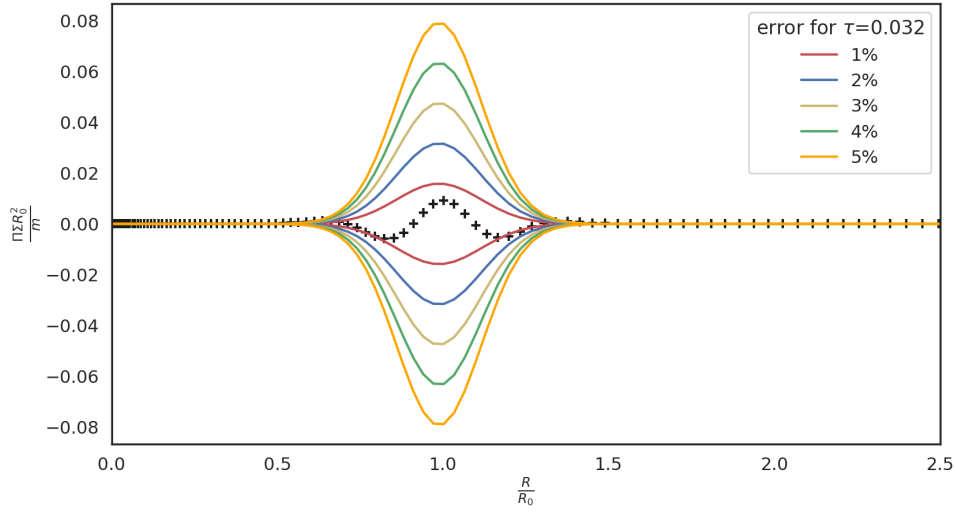
Figure 2.3: Errors of the numerical solution in comparison to analytical solution for $\tau = 0.032$ with the initial mass ring located at $R_0 = 23.6R_{\mathrm{g}}$. The errors marked by black crosses and evaluated relative to the $1\% - 5\%$ multiple of the absolute value of the coresponding surface density.
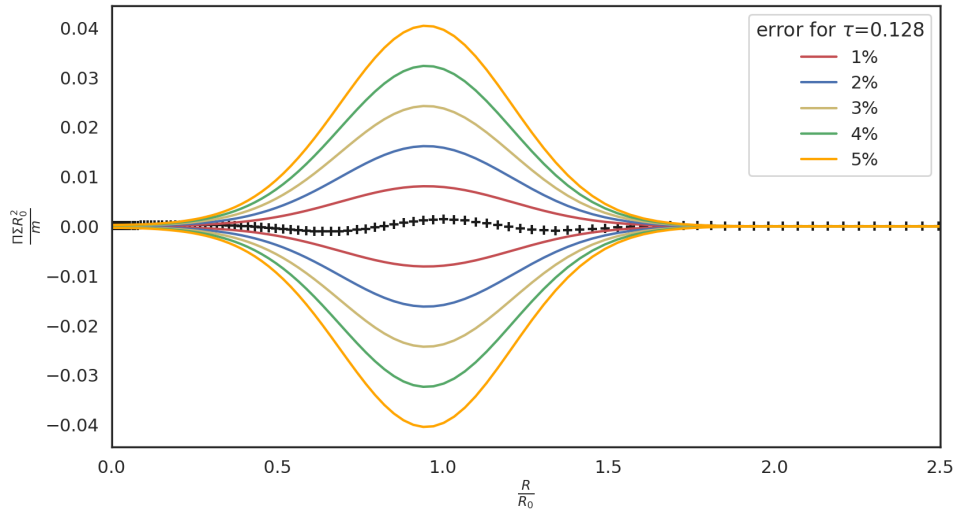
Figure 2.4: Errors of the numerical solution in comparison to analytical solution for $\tau = 0.128$ with the initial mass ring located at $R_0 = 23.6R_{\mathrm{g}}$. The errors marked by black crosses and evaluated relative to the $1\% - 5\%$ multiple of the absolute value of the coresponding surface density.
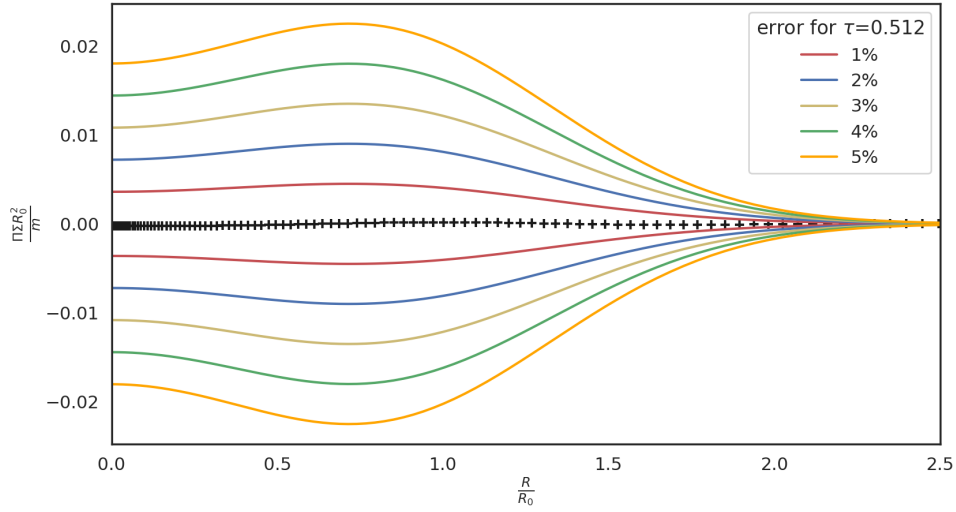
Figure 2.5: Errors of the numerical solution in comparison to analytical solution for $\tau = 0.512$ with the initial mass ring located at $R_0 = 23.6R_{\mathrm{g}}$. The errors marked by black crosses and evaluated relative to the $1\% - 5\%$ multiple of the absolute value of the coresponding surface density.
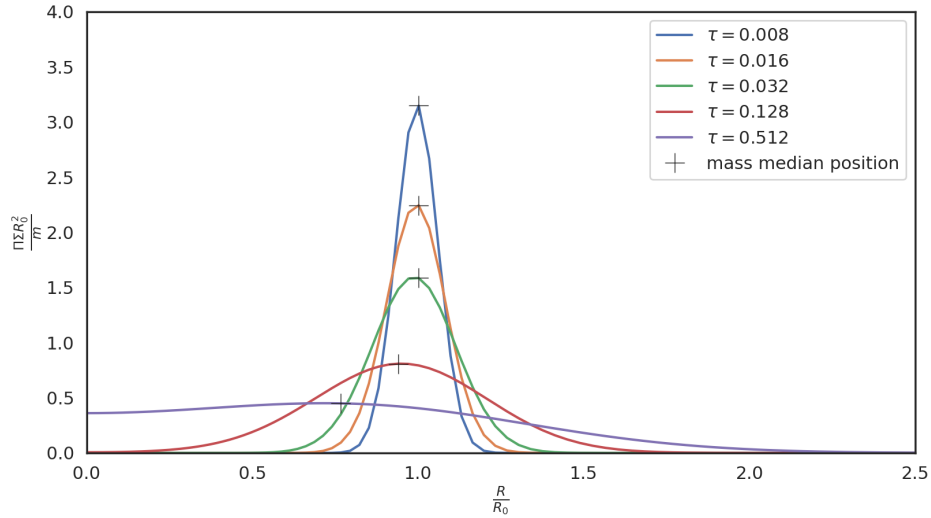
Figure 2.6: Numerical solution to the diffusion equation (1.40) describing the evolution of the surface density profile of the initial mass ring located at $R_0 = 23.6R_{\mathrm{g}}$ with boundary conditions $\Sigma(R_{\mathrm{inner}} = 0, t) = \Sigma(R_{\mathrm{outer}}, t) = 0$. Black crosses mark the margin for the half of mass of the accretion disc at a given time.
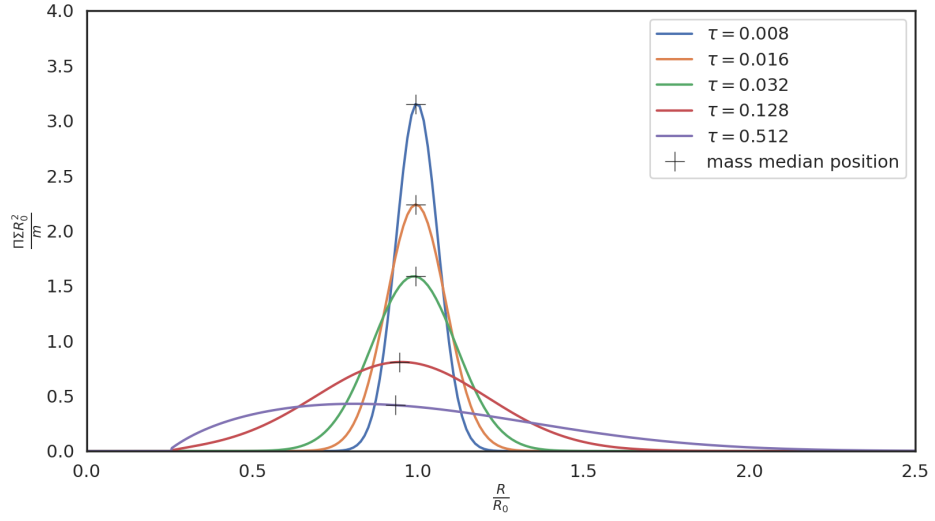
Figure 2.7: Numerical solution to the diffusion equation (1.40) describing the evolution of the surface density profile of the initial mass ring located at $R_0 = 23.6 R_{\mathrm{g}}$ with boundary conditions $\Sigma(R_{\mathrm{inner}} = 6R_{\mathrm{g}}, t) = \Sigma(R_{\mathrm{outer}}, t) = 0$. Black crosses mark the margin for the half of mass of the accretion disc at a given time.
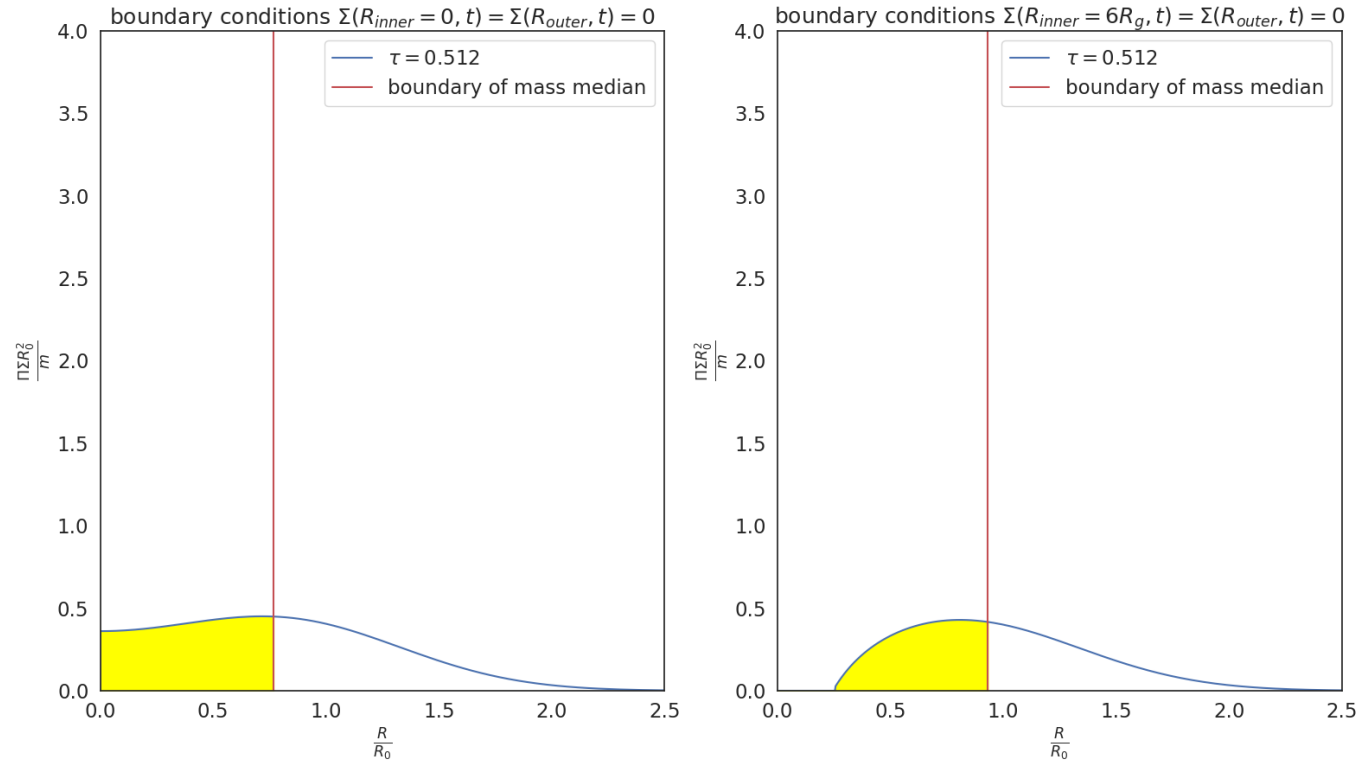
Figure 2.8: The surface density profile difference in case of different boundary conditions of the studied accretion disc – $\Sigma(R_{\text{inner}} = 0, t) = \Sigma(R_{\text{outer}}, t) = 0$ (left panel) and $\Sigma(R_{\text{ISCO}} = 6R_{\text{g}}, t) = \Sigma(R_{\text{outer}}, t) = 0$ (right panel) with the initial mass ring located at $R_0 = 23.6R_{\text{g}}$. Red lines mark the mass median boundary of a given accretion disc at a given time.

2.3 Spectral line profile calculation

Radiation flux F_ν^i with $i = 1, 2, 3$ is a vector entity such as $F_\nu^i \, dS_i$ and equals the energy flow net rate of radiation in frequency interval $(\nu, \nu + d\nu)$ across arbitrary surface element dS per unit time and frequency. In its most general form we can describe the monochromatic (/ specific) radiation flux by the following formula [Hubený and Mihalas, 2014]

$$F_\nu^i = \int I_\nu(n_x, n_y, n_z) \, n^i \, d\Omega, \; i = 1, 2, 3, \tag{2.17}$$

integrating over all solid angles.

We adopt the axial symmetry of the studied systems. We write the formula for overall observed monochromatic flux coming from a gaseous ring surrounding the central body as

$$F_{\text{ring-observed}} = \int_0^{2\pi} I_{\text{observed}} \, d\varphi. \tag{2.18}$$

In Newtonian case we set the observed intensity I_{observed} equal to the emitted one I_{emitted}. In special relativistic and general relativistic scenario we use the equation (1.70) and rewrite the equation (2.18) as

$$F_{\text{ring-observed}} = \int_0^{2\pi} I_{\text{emitted}} \frac{\nu_{\text{observed}}^3}{\nu_{\text{emitted}}^3} \, d\varphi, \tag{2.19}$$

whereas we use the respective special relativistic and general relativistic redshift factors (1.76) and (1.81) in form $g(R = \text{const}_1, \varphi, I = \text{const}_2)$ variable only in φ. For the initial radiation intensity profile we chose the delta distribution representation

$$I_\nu \approx \delta(\nu - \nu_0) \tag{2.20}$$

assuming the ring radiates at one chosen frequency ν_0 and approximating the delta distribution as

$$\delta(\nu - \nu_0) \approx \lim_{a \to 0} \exp\left(- \left(\frac{\nu - \nu_0}{a} \right)^2 \right). \tag{2.21}$$

Now if we want to model total value of flux from the accretion disc as a whole we can do so by splitting it in numerous infinitesimal rings, calculate their respective monochromatic fluxes and add them together using the following relation

$$F_{\text{accretion disc-observed}} = \int \int I_{\text{observed}} dS = \int_{R_{\text{inner}}}^{R_{\text{outer}}} \int_0^{2\pi} I_{\text{observed}} R dR d\varphi \tag{2.22}$$

The argumentation and method for calculating of the value of total flux is similar as for the ring expect for the fact one must let the special relativistic and general relativistic redshift factor as $g(R, \varphi, I)$ a function of R, φ and I. We describe the initial radiation intensity profile using the delta distribution

$$I_\nu \approx \delta(\nu - \nu_0) \frac{1}{R^p} \tag{2.23}$$

assuming the entire disc radiates at the same chosen frequency ν_0 and using the same approximation for the delta distribution as in the equation (2.21). Depending on the parameter of the value of the outer radius of the corona surrounding the accretion disc R_c we choose the parameter $q = 0$ for $R < R_c$, $q = 2$ for $R \approx R_c$ and $q = 3$ for $R > R_c$ [Fabian et al., 1989b].

2.4 The spectral line profiles from gaseous rings and accretion discs in Keplerian rotation

The major motivation standing behind the study of the spectral line profiles lies in the possibility to infer the object's inclination, to set constraints on the size of the radiating region, the spin of the central body etc. In this section we present the spectral line profiles of radiation coming from rotating rings in Newtonian, special relativistic and general relativistic approximation using the redshift factor formulae (1.78), (1.76) and (1.81) respectively. We also show the spectral line profiles of radiation coming from accretion disc taking the general relativistic approximation (1.81).

We assume the disc to be geometrically thin with dominant azimuthal velocity component whereas the radial and the vertical components can be neglected ($v_\varphi \gg v_R \gg v_z$) as mentioned in section 1.2. We do not take into account the presence of magnetic field as it would change the prescription for the kinematic viscosity (1.58). We study the properties of radiation distributed isotropically. We assume the central object to be a slowly rotating or non-rotating super-massive black hole with no electrical charge, described by the Schwarzschild solution (1.80).

The following Figures 2.9 to 2.11 show the spectral line profiles for a mass ring at $6R_{\mathrm{g}}$ in Newtonian, special relativistic and general relativistic approximation respectively normalized by two methods as $\int F_\nu \, dv = 1/(/ \int F_\nu \, dg = 1)$ and to the height of the blueshifted peak of a given spectral line. The Figure 2.12 shows the spectral line profiles for a gaseous ring at $10R_{\mathrm{g}}$, $15R_{\mathrm{g}}$, $30R_{\mathrm{g}}$, $50R_{\mathrm{g}}$ and $80R_{\mathrm{g}}$ in general relativistic approximation using the normalization $\int F_\nu \, dg = 1$. The Figure 2.13 shows the spectral line profiles for an accretion disc with varying parameters R_{inner}, R_{outer} and I in general relativistic approximation using the normalization $\int F_\nu \, dg = 1$.
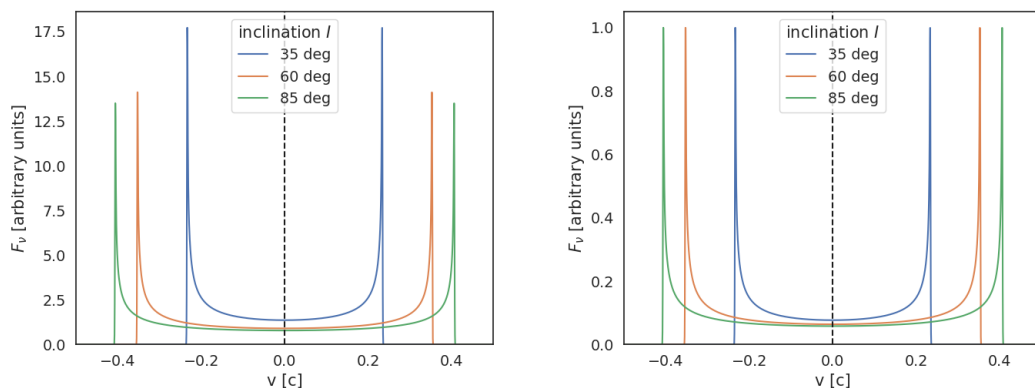
Figure 2.9: The spectral line profile for a gaseous ring at $6R_{\mathrm{g}}$ in Newtonian approximation normalized: on the left – such as $\int F_\nu \, dv = 1$, on the right – to the height of the blueshifted peak of a given spectral line. Black dotted line marks the intrinsic frequency.
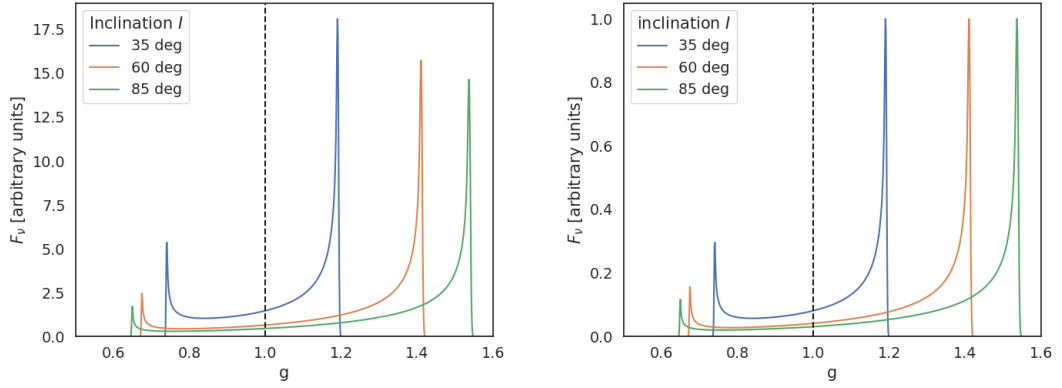
Figure 2.10: The spectral line profiles for a gaseous ring at $6R_{\mathrm{g}}$ in special relativistic approximation normalized: on the left – such as $\int F_\nu \, dg = 1$, on the right – to the height of the blueshifted peak of a given spectral line. Black dotted line marks the intrinsic frequency.
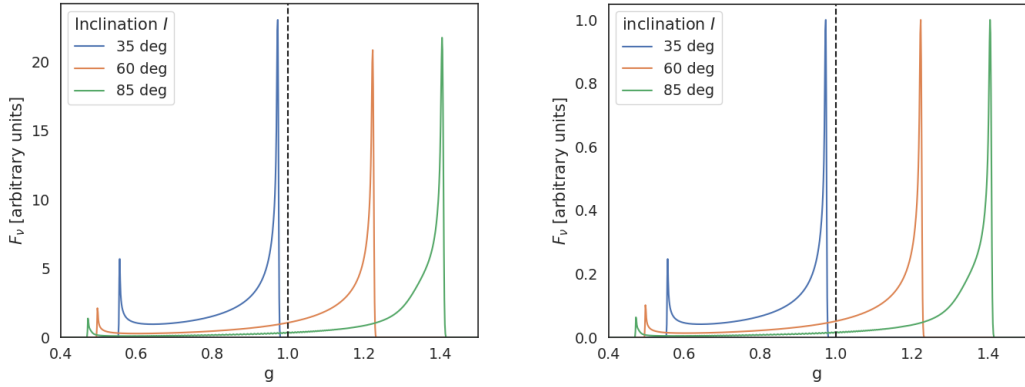
Figure 2.11: The spectral line profiles for a gaseous ring at $6R_{\mathrm{g}}$ in general relativistic approximation normalized: on the left – such as $\int F_\nu \, dg = 1$, on the right – to the height of the blueshifted peak of a given spectral line. Black dotted line marks the intrinsic frequency.

Based on the Figures 2.9 – 2.11 we notice that the bigger the inclination is the more the spectral line will be shifted. In the Figure 2.9 we can observe the symmetrical redshifted (the material is receding) and blueshifted (the material is closing in) peaks of the spectral lines. The spectral line profiles calculated in special relativistic and general relativistic approximation show an asymmetry in the height of the redshifted and blueshifted peak caused by using the formula (1.70) which is a direct consequence of the Liouville's theorem (1.65) and the observed effect is called relativistic aberration (see Figure 2.10). The major difference between the Figures 2.9, 2.10 compared to the Figure 2.11 lies within the gravitational redshift that causes the spectral line to be shifted to lower energy as well as the light bending effect. In the Figure 2.11 the spectral line with the inclination 35 deg is an example of a spectral line that has been fully redshifted due to the gravitational redshift. As we change the inclination angle to 60 and 85 deg the Doppler broadening causes the line not to be fully redshifted anymore.

We notice that both the gravitational redshift and the light bending effect get weaker as the rotating rings are located further from the central black hole as well as the fact that the blueshifted peak of the spectral line is higher the less the radiation source is inclined (see Figure 2.12). Generally the broadening caused due to the Doppler shift gets weaker because the Keplerian velocity of the rotating ring goes as $\propto R^{-\frac{1}{2}}$ (see Figures 2.11 and 2.12, in case of general relativistic approximation).
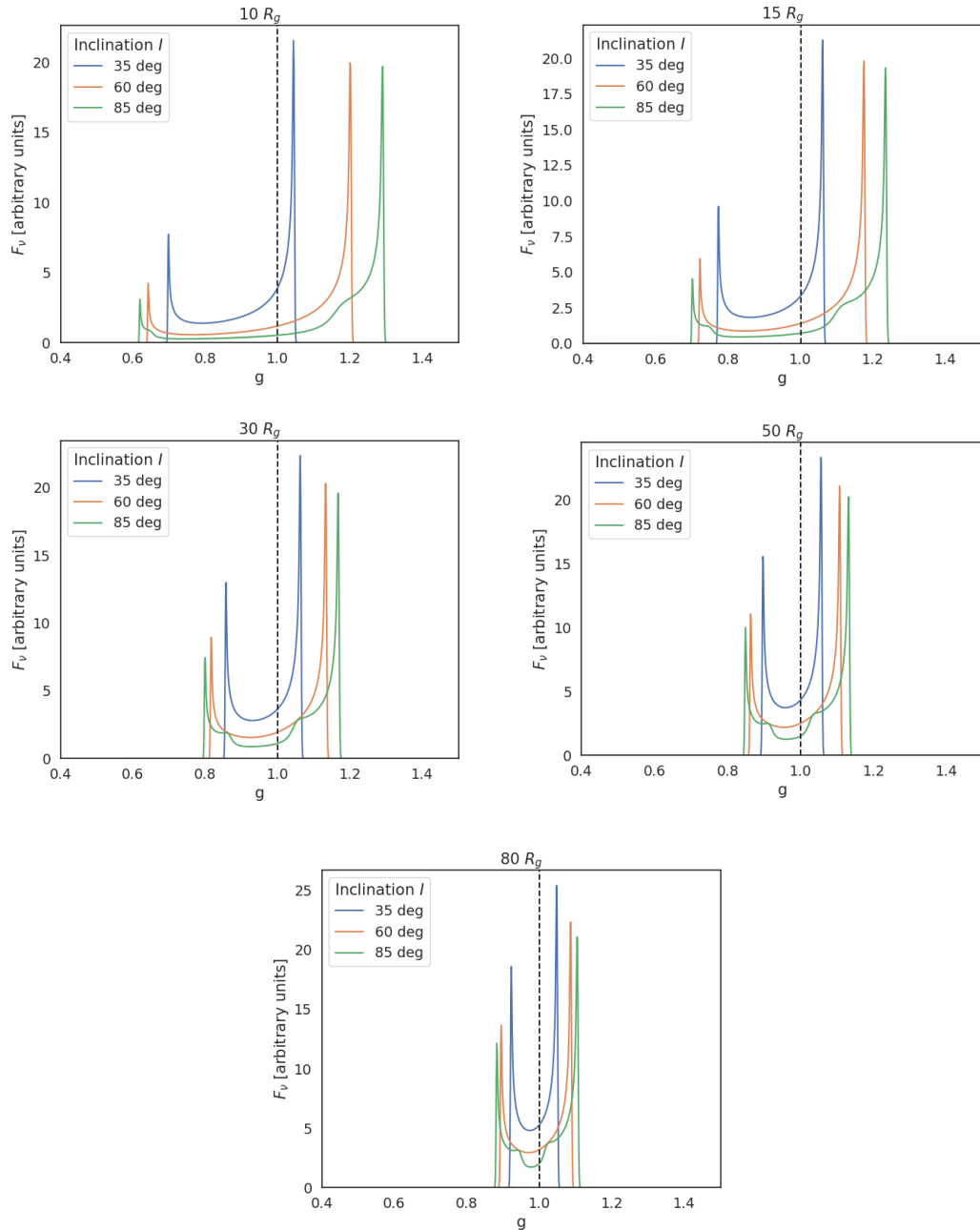
Figure 2.12: The spectral line profiles for a gaseous ring at $10R_{\mathrm{g}}$, $15R_{\mathrm{g}}$, $30R_{\mathrm{g}}$, $50R_{\mathrm{g}}$ and $80R_{\mathrm{g}}$ in general relativistic approximation normalized such as $\int F_{\nu}\, dg = 1$. Black dotted line marks the intrinsic frequency.
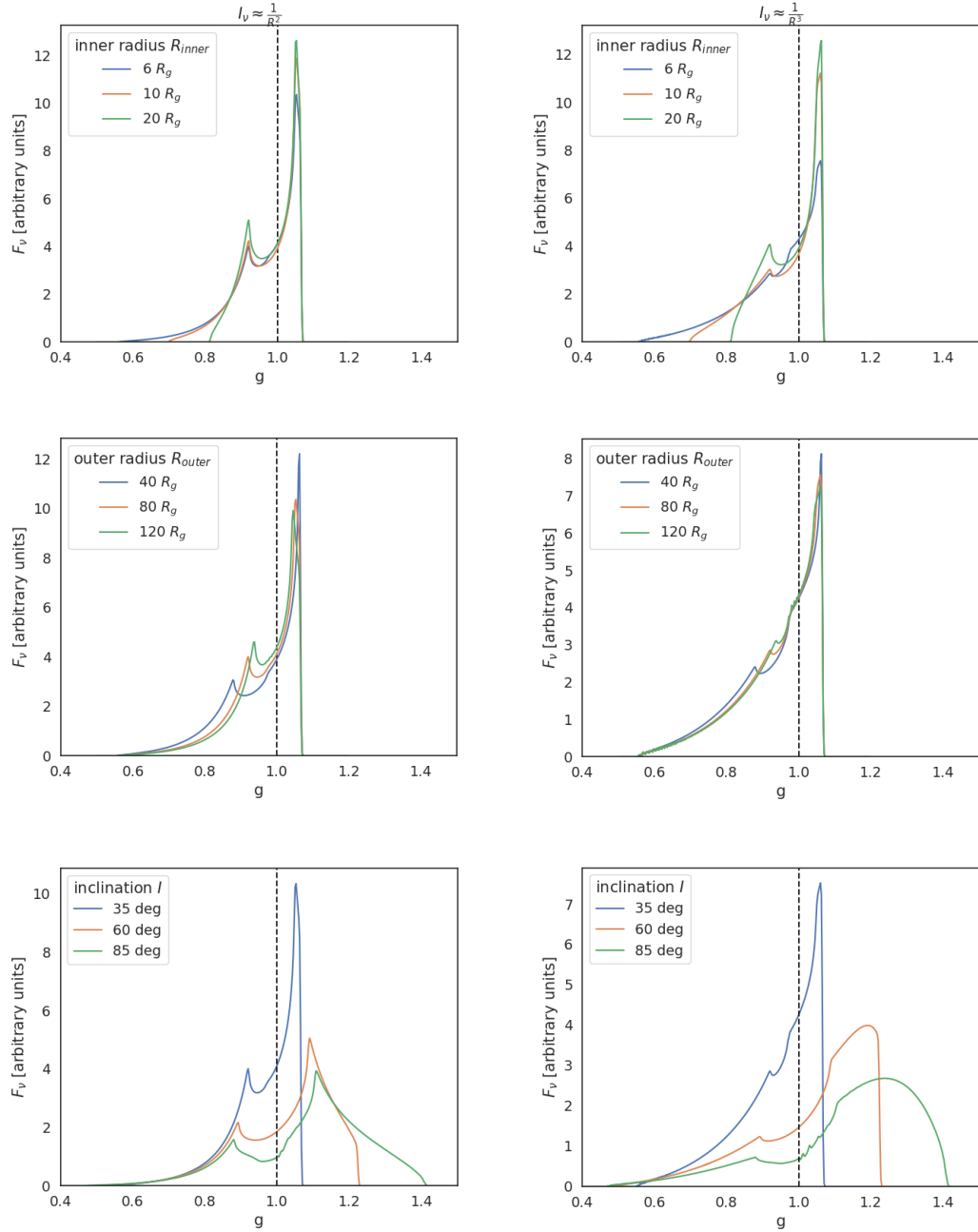
Figure 2.13: The spectral line profiles for an accretion disc in general relativistic approximation with the initial radiation intensity $I_\nu \approx \frac{1}{R^2}$ (left panel) and $I_\nu \approx \frac{1}{R^3}$ (right panel) normalized such as $\int F_\nu\, dg = 1$. The parameters are $R_{\text{inner}} = 6R_{\text{g}}$, $R_{\text{outer}} = 80R_{\text{g}}$ and $I = 36\,\text{deg}$, if not stated otherwise. Black dotted line marks the intrinsic frequency.

Varying the outer radius of the accretion disc shows that for bigger values the spectral line profile tends to approach the intrinsic frequency (see the middle two plots in the Figure 2.13). We also notice how the shape of the wings of the spectral line profiles depends on the value of the inner radius of the accretion disc (see the first two plots in the Figure 2.13). The spectral line profile for the initial radiation intensity $\approx \frac{1}{R^2}$ seems to be more sensitive to the changes of the outer radius of the accretion disc rather than the inner radius. On the contrary, for

the initial radiation intensity $\approx \frac{1}{R^3}$, it is the inner accretion radius that mostly contributes to the spectral line profile changes. The bigger the inclination gets the more we can expect the spectral line profile to be shifted (see the last two plots in the Figure 2.13).

2.5 The spectral line profiles and their centroid energy in scenario of a tidally disrupted star

In order to describe the spectral line profile features of radiation coming from the central area of galactic nuclei with a massive object such as a super-massive black hole we use general relativistic framework. On the other hand we do not develop any kind of consistent realistic micro-physical approach. The resulting spectral line profiles in this chapter are limited by the following condition

$$R_{\text{tidal}} \leq 50R_{\text{g}}. \tag{2.24}$$

The surface density profile of the initial mass ring located at the tidal radius $R_0 = R_{\text{tidal}}$ will be evolving according to the equation (1.40), i.e. the value of the outer radius of the accretion disc will be more than $2.5\times$that of the position of the initial mass ring (see e.g. Figure 1.2). We have chosen the tidal radius threshold value not only to enable the calculations to be stable and relatively fast. The main reason was to capture the spectral line profile time evolution after the occurrence of the tidal disruption in the close proximity of the central object in the order of tens of R_{g} because the relativistic effects are negligible farther away.

The initial idea is to map the spectral line profile time evolution. We assume the radiation to be reflected by the accretion disc whose surface density profile is evolving. Therefore because the accretion disc is changing its radius the area which could be potentially used to reflect the observed radiation is also changing.

In our system set-up we assume the star to be of a solar type, meaning $M_* = 1M_{\odot}$ and $R_* = 1R_{\odot}$, and we keep varying the mass of the central object, so that we cover the interval given as (2.24), see Table 2.1. The Table 2.2 sets the constraints on the size of the accretion disc in a given system set-up. To calculate the constraints of the size of the accretion discs we used the boundary condition $\Sigma(R_{\text{ISCO}} = 6R_{\text{g}}, t) = \Sigma(R_{\text{outer}}, t) = 0$ forcing the surface density profile to be zero under the ISCO radius.

To calculate the order of the temperature profile of the accretion disc in Table 2.1 we used the equation (1.55) whereas we used the formula describing the accretion luminosity (1.54) to get the respective value of the accretion rate under the assumption that it is limited by the Eddington luminosity of the accreted star (2.16). The kinematic viscosity values in the Table 2.1 correspond to values of C_ν given by the equation (2.15). The respective values of tidal radius in the Table 2.1 were calculated using the equation (1.7). At time $\tau = 0$ we set $R_{\text{inner}} = R_{\text{outer}} = R_{\text{tidal}}$ as we are investigating the initial mass ring (see Table 2.2). The values of R_{inner} and R_{outer} at time $\tau \neq 0$ in the Table 2.2 result from the numerical solution of the equation describing the evolution of the surface density profile of the accretion disc given as (1.40).

The Figures 2.14 – 2.16, 2.17 – 2.19, 2.20 – 2.22 and 2.23 – 2.25 depict the spectral line profile evolution and position of their centroid energy (mean values

of energy in a given spectral line) for system set-up A, B, C and D respectively using the normalization $\int F_\nu \, dg = 1$.

Table 2.1: List of studied system set-up

System set-up	star		central body	$T[K]$	$\nu[\frac{R_\mathrm{g}^2}{s}]$	$R_\mathrm{tidal}[R_\mathrm{g}]$
	$M_*[M_\odot]$	$R_*[R_\odot]$	$M_\mathrm{BH}[M_\odot]$			
A	1	1	1.5×10^6	$\approx 10^3$	1.2×10^{-11}	45.4
B	1	1	2×10^6	$\approx 10^3$	9.3×10^{-12}	37.5
C	1	1	4×10^6	$\approx 10^3$	4.6×10^{-12}	23.6
D	1	1	1×10^7	$\approx 10^3$	1.9×10^{-12}	12.8

Table 2.2: Parameters describing the size of the initial mass rings and accretion discs for system set-up A, B, C and D

τ	D		C		B		A	
	$R_\mathrm{tidal}= 12.8\ R_\mathrm{g}$		$R_\mathrm{tidal}= 23.6\ R_\mathrm{g}$		$R_\mathrm{tidal}= 37.5\ R_\mathrm{g}$		$R_\mathrm{tidal}= 45.4\ R_\mathrm{g}$	
	$R_\mathrm{inner}[R_\mathrm{g}]$	$R_\mathrm{outer}[R_\mathrm{g}]$	$R_\mathrm{inner}[R_\mathrm{g}]$	$R_\mathrm{outer}[R_\mathrm{g}]$	$R_\mathrm{inner}[R_\mathrm{g}]$	$R_\mathrm{outer}[R_\mathrm{g}]$	$R_\mathrm{inner}[R_\mathrm{g}]$	$R_\mathrm{outer}[R_\mathrm{g}]$
0	12.8	12.8	23.6	23.6	37.5	37.5	45.4	45.4
0.008	8.5	17.0	15.7	31.3	24.9	49.9	30.3	60.1
0.016	6.7	18.7	12.4	34.4	19.8	54.7	24.0	66.4
0.032	6.0	21.2	8.0	38.4	12.8	61.6	15.5	74.4
0.128	6.0	28.6	6.0	52.5	6.0	83.0	6.0	100.8
0.512	6.0	42.6	6.0	78.1	6.0	124.4	6.0	150.4
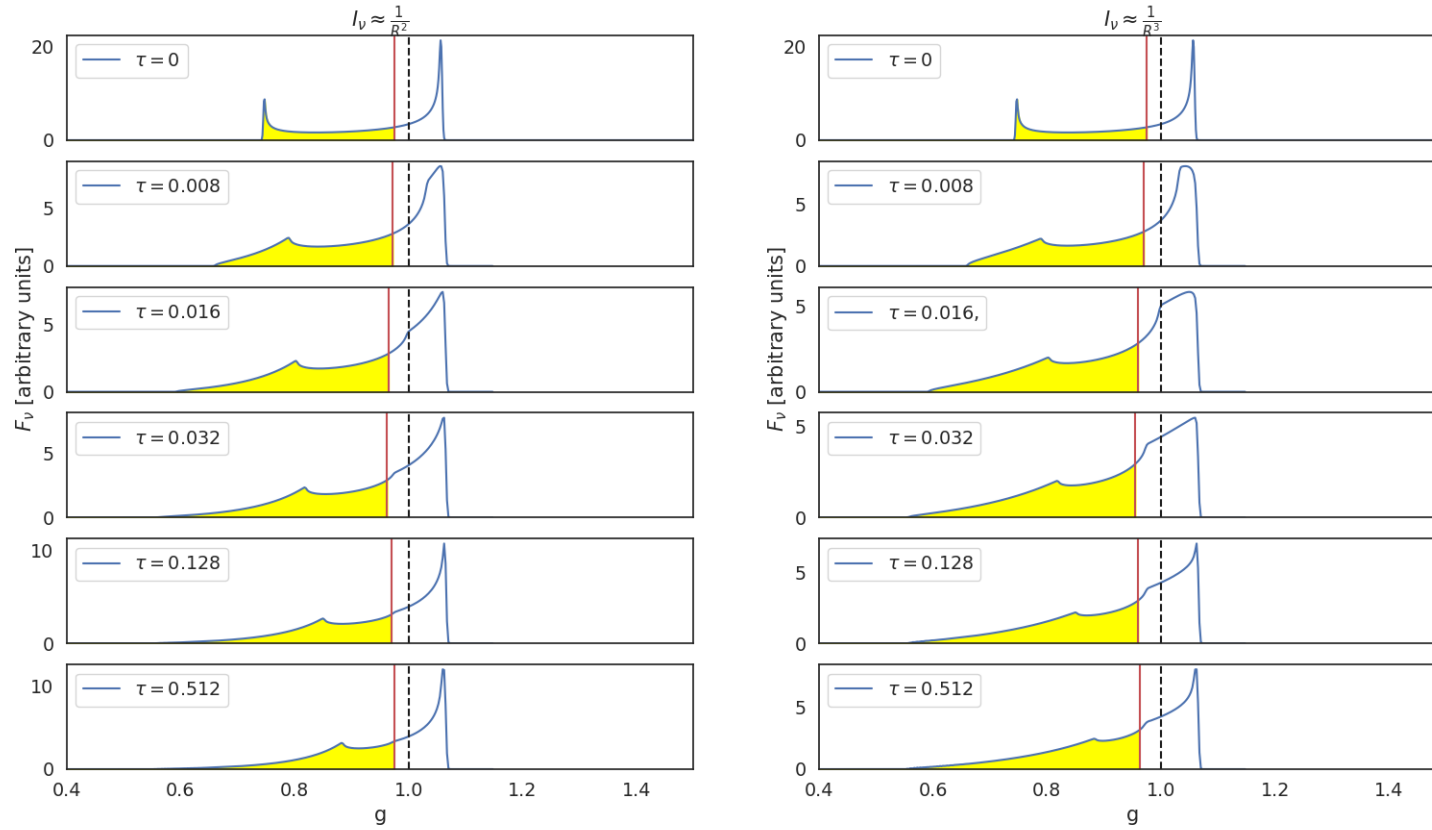
Figure 2.14: Spectral line profile evolution for the system set-up D with the inclination $I = 35$ deg, with the initial radiation intensity $I_\nu \approx \frac{1}{R^2}$ (left panel) and $I_\nu \approx \frac{1}{R^3}$ (right panel). Black dotted line marks the intrinsic frequency, red line marks the centroid energy of a given spectral line.
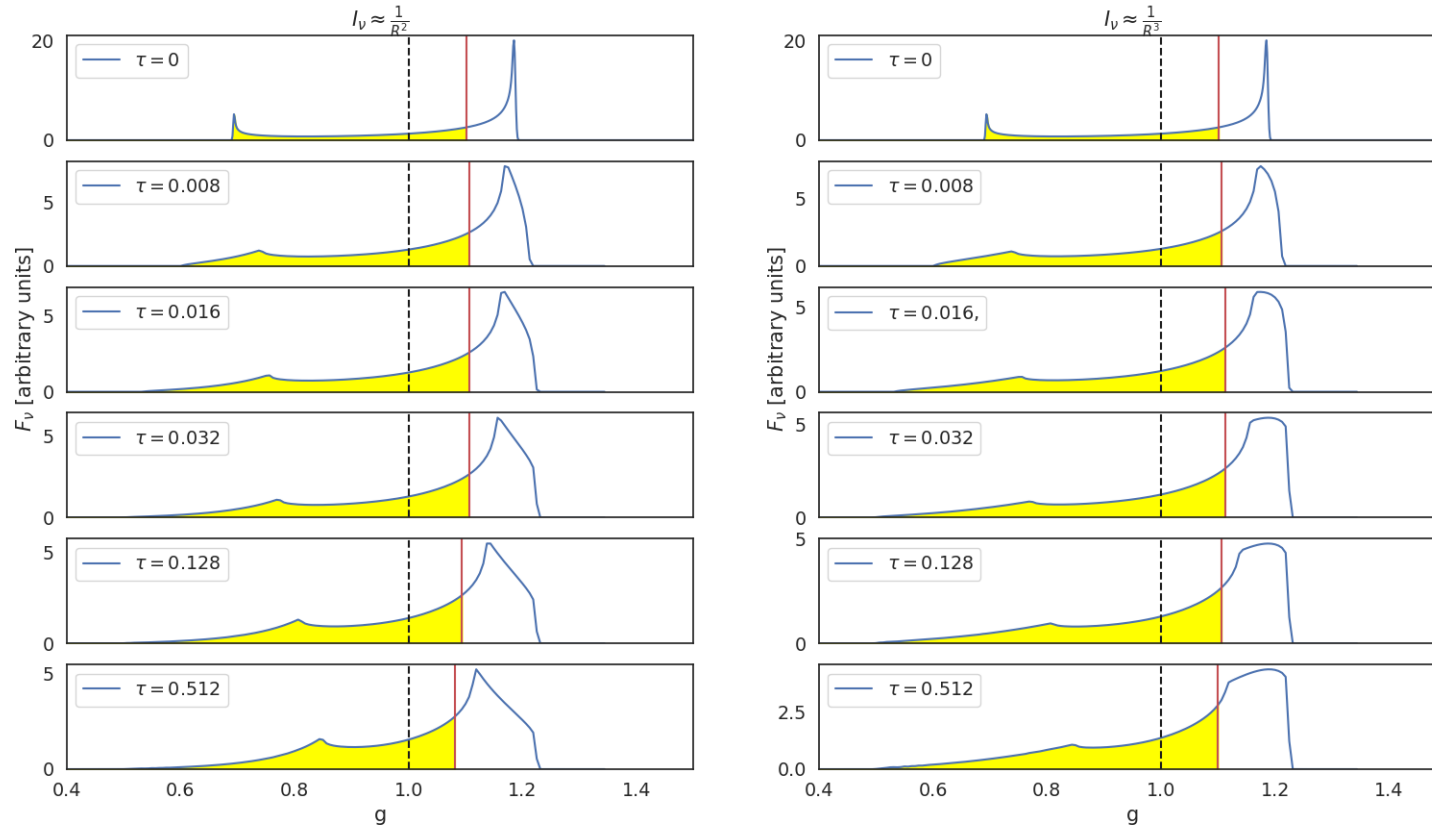
Figure 2.15: Spectral line profile evolution for the system set-up D with the inclination $I = 60$ deg, with the initial radiation intensity $I_\nu \approx \frac{1}{R^2}$ (left panel) and $I_\nu \approx \frac{1}{R^3}$ (right panel). Black dotted line marks the intrinsic frequency, red line marks the centroid energy of a given spectral line.
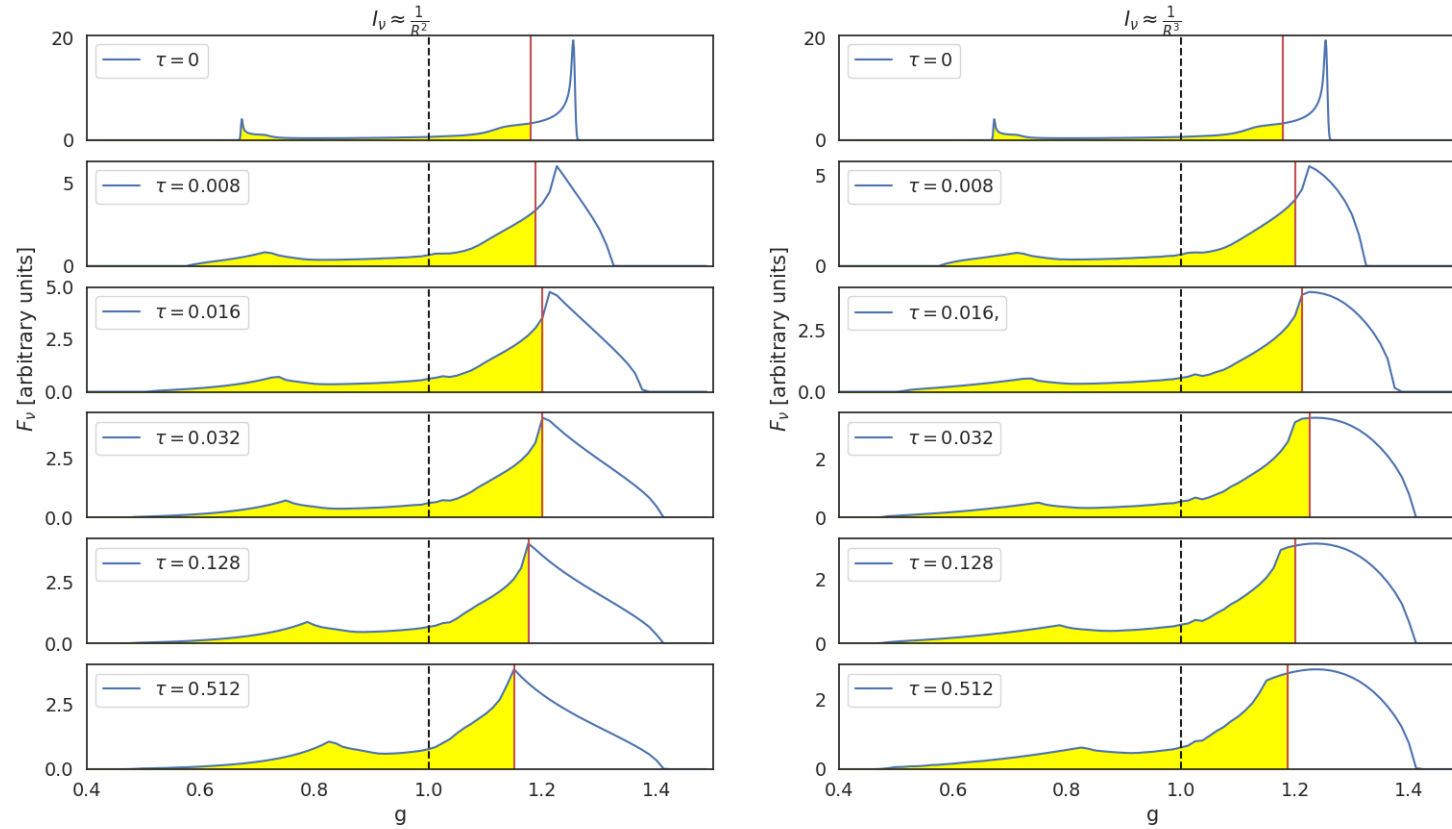
Figure 2.16: Spectral line profile evolution for the system set-up D with the inclination $I = 85$ deg, with the initial radiation intensity $I_\nu \approx \frac{1}{R^2}$ (left panel) and $I_\nu \approx \frac{1}{R^3}$ (right panel). Black dotted line marks the intrinsic frequency, red line marks the centroid energy of a given spectral line.
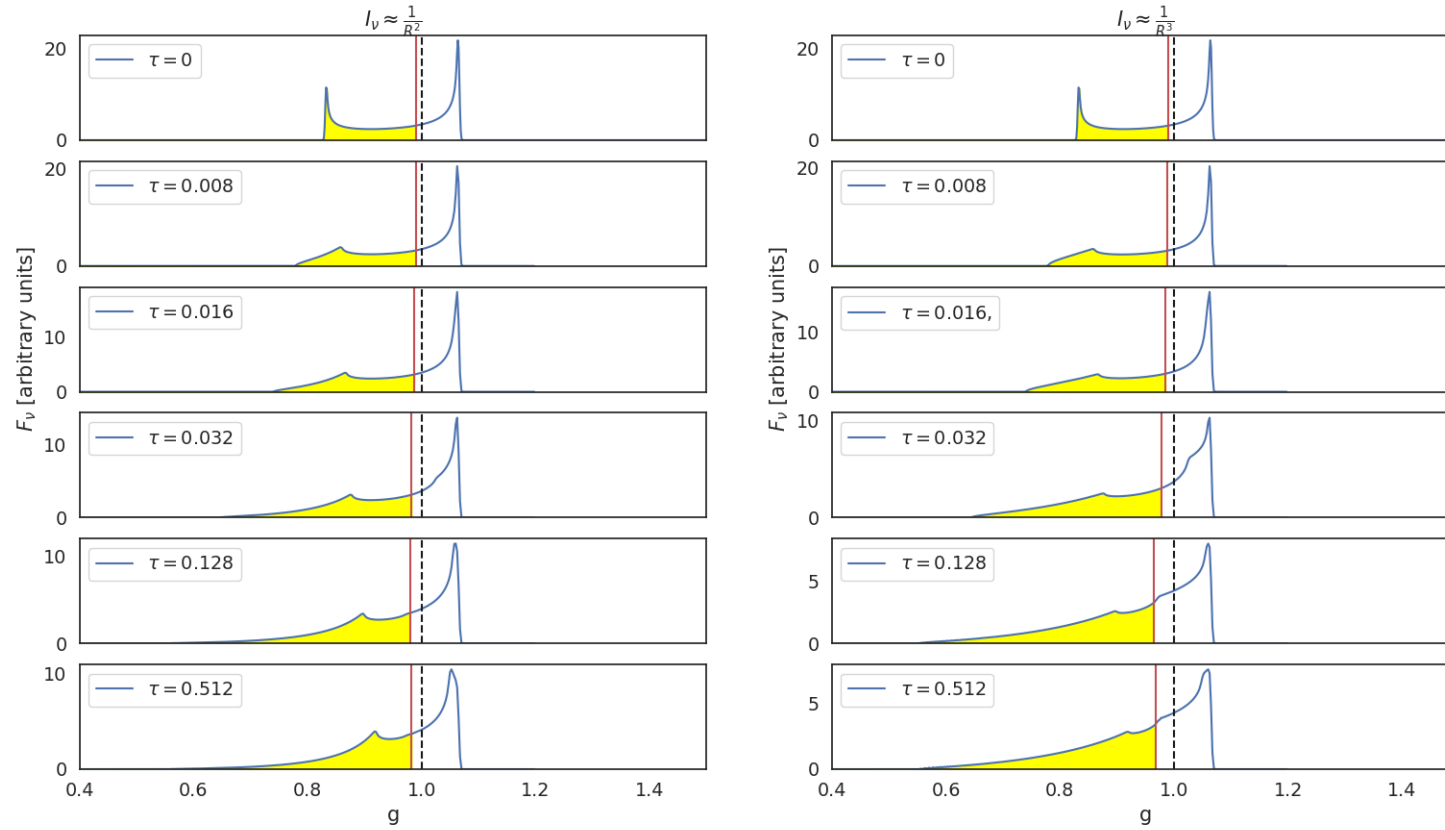
Figure 2.17: Spectral line profile evolution for the system set-up C with the inclination $I = 35$ deg, with the initial radiation intensity $I_\nu \approx \frac{1}{R^2}$ (left panel) and $I_\nu \approx \frac{1}{R^3}$ (right panel). Black dotted line marks the intrinsic frequency, red line marks the centroid energy of a given spectral line.
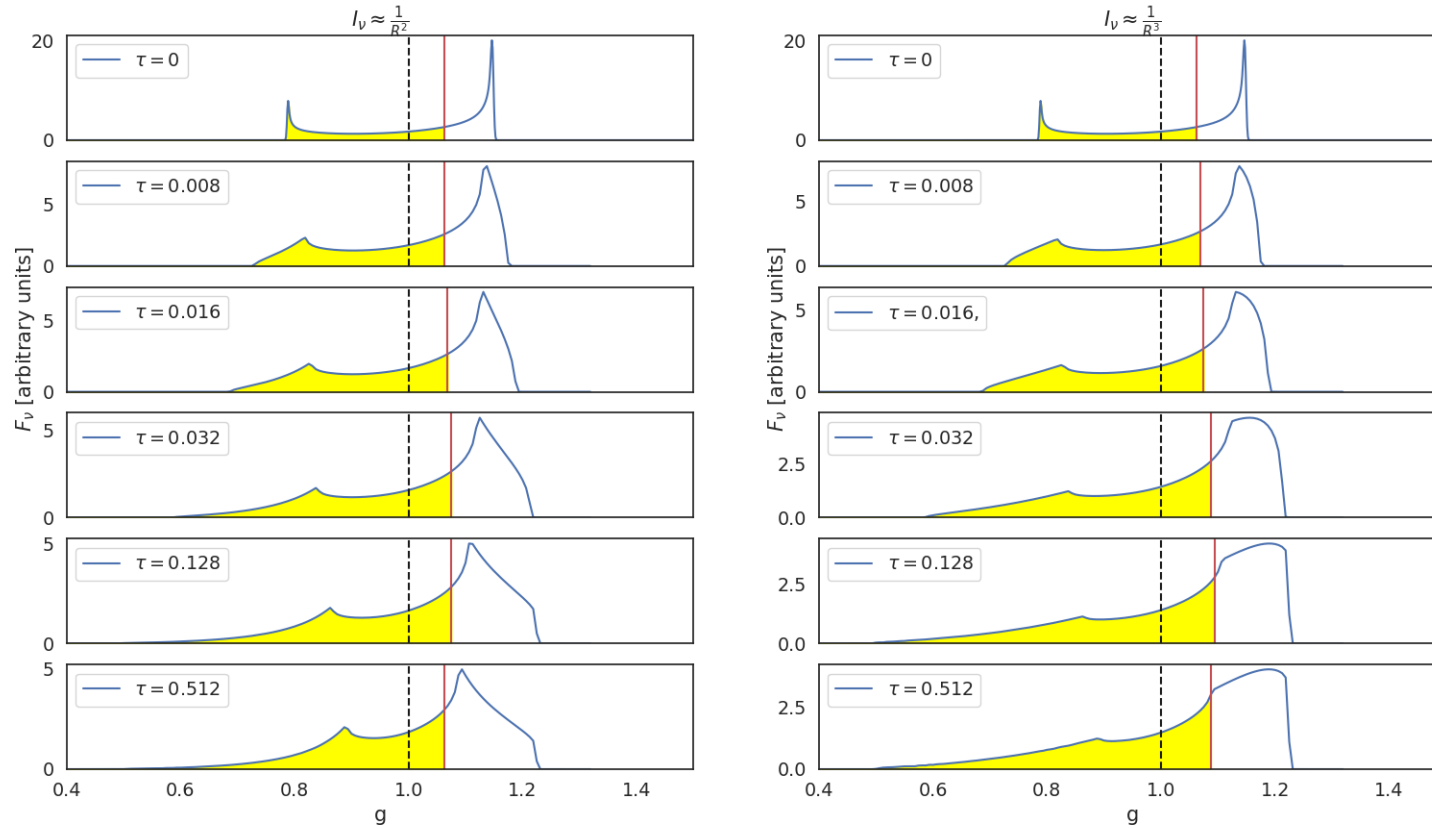
Figure 2.18: Spectral line profile evolution for the system set-up C with the inclination $I = 60$ deg, with the initial radiation intensity $I_\nu \approx \frac{1}{R^2}$ (left panel) and $I_\nu \approx \frac{1}{R^3}$ (right panel). Black dotted line marks the intrinsic frequency, red line marks the centroid energy of a given spectral line.
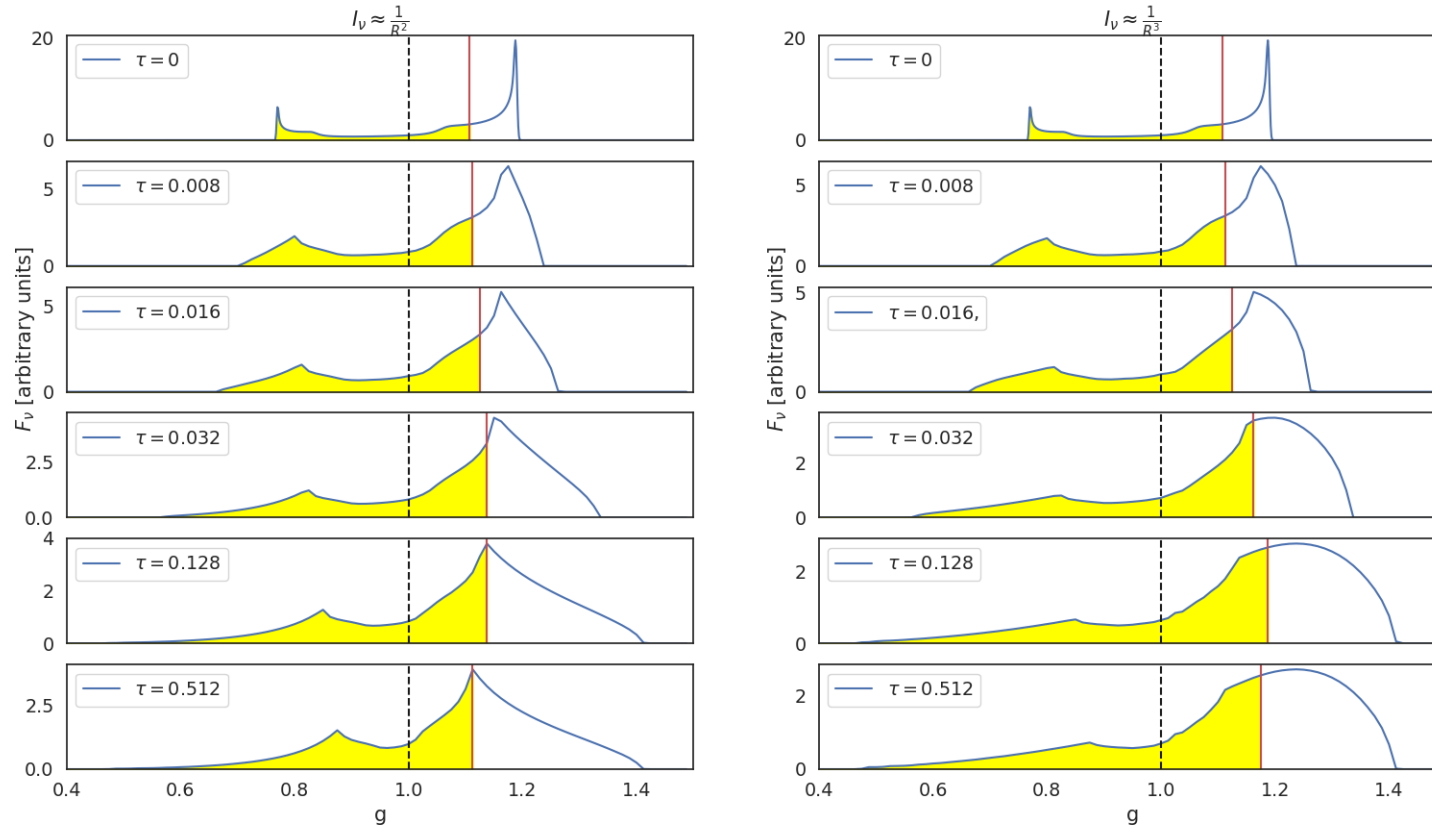
Figure 2.19: Spectral line profile evolution for the system set-up C with the inclination $I = 85$ deg, with the initial radiation intensity $I_\nu \approx \frac{1}{R^2}$ (left panel) and $I_\nu \approx \frac{1}{R^3}$ (right panel). Black dotted line marks the intrinsic frequency, red line marks the centroid energy of a given spectral line.
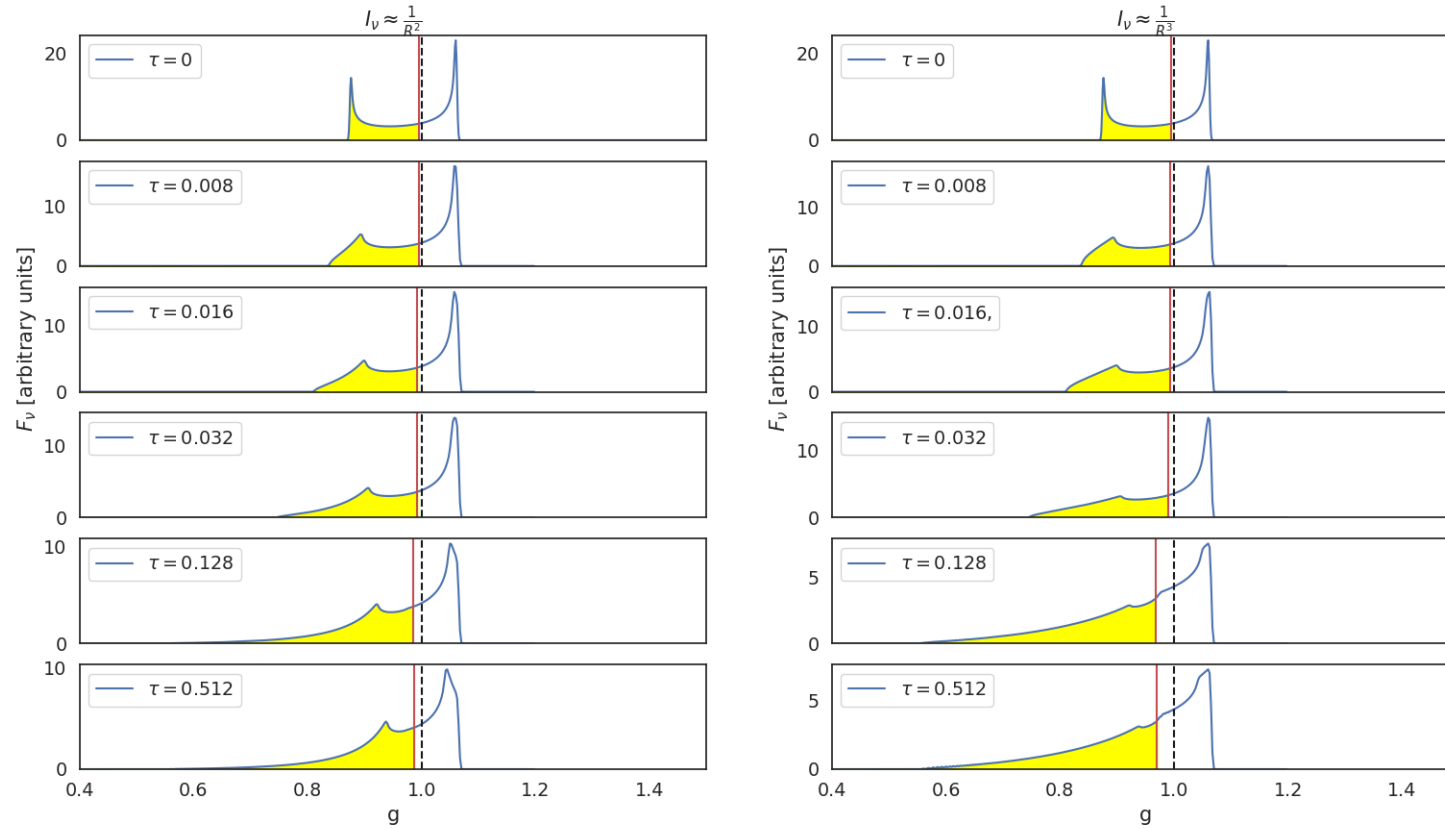
Figure 2.20: Spectral line profile evolution for the system set-up B with the inclination $I = 35$ deg, with the initial radiation intensity $I_\nu \approx \frac{1}{R^2}$ (left panel) and $I_\nu \approx \frac{1}{R^3}$ (right panel). Black dotted line marks the intrinsic frequency, red line marks the centroid energy of a given spectral line.
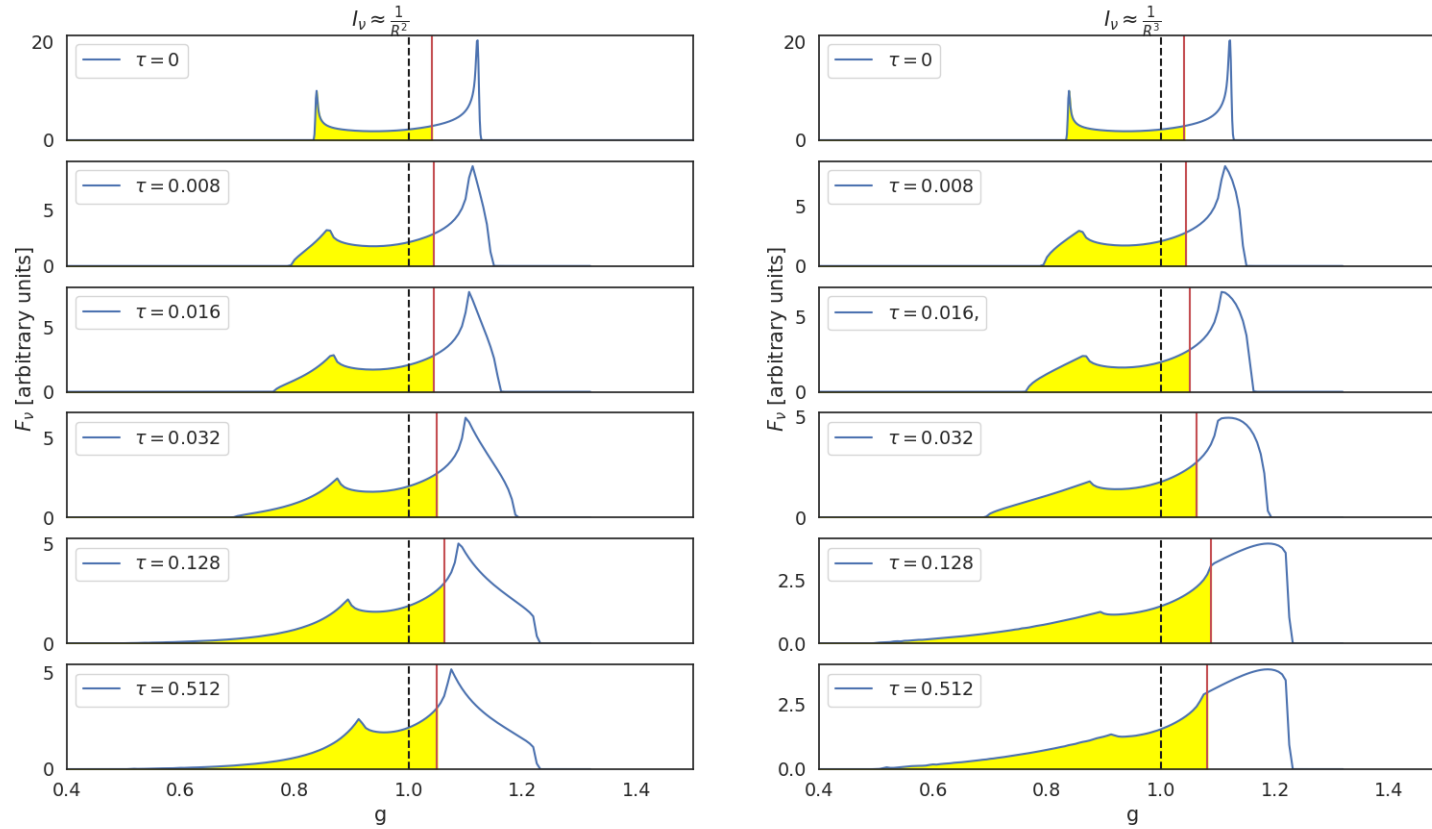
Figure 2.21: Spectral line profile evolution for the system set-up B with the inclination $I = 60$ deg, with the initial radiation intensity $I_\nu \approx \frac{1}{R^2}$ (left panel) and $I_\nu \approx \frac{1}{R^3}$ (right panel). Black dotted line marks the intrinsic frequency, red line marks the centroid energy of a given spectral line.
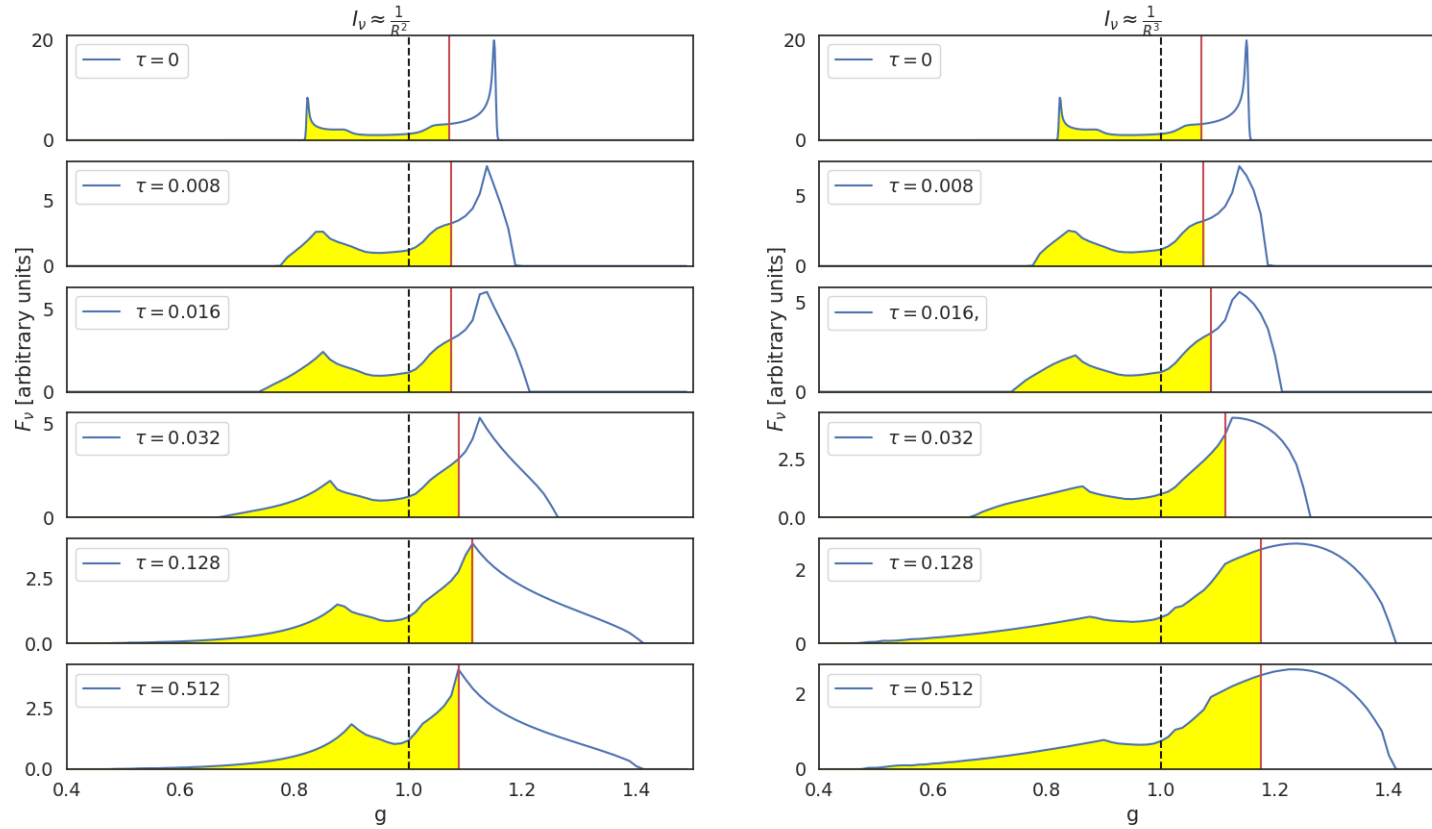
Figure 2.22: Spectral line profile evolution for the system set-up B with the inclination $I = 85$ deg, with the initial radiation intensity $I_\nu \approx \frac{1}{R^2}$ (left panel) and $I_\nu \approx \frac{1}{R^3}$ (right panel). Black dotted line marks the intrinsic frequency, red line marks the centroid energy of a given spectral line.
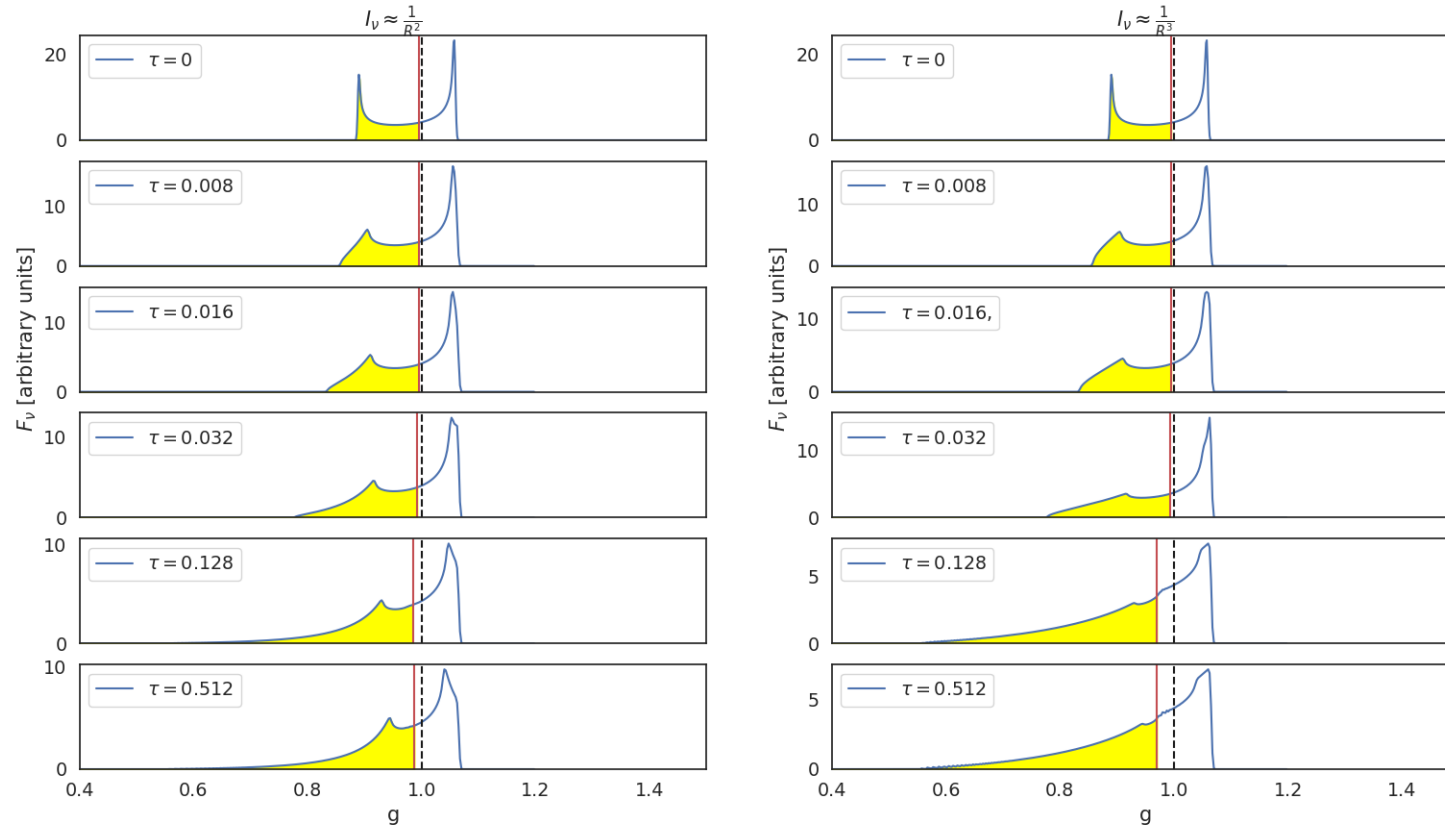
Figure 2.23: Spectral line profile evolution for the system set-up A with the inclination $I = 35$ deg, with the initial radiation intensity $I_\nu \approx \frac{1}{R^2}$ (left panel) and $I_\nu \approx \frac{1}{R^3}$ (right panel). Black dotted line marks the intrinsic frequency, red line marks the centroid energy of a given spectral line.
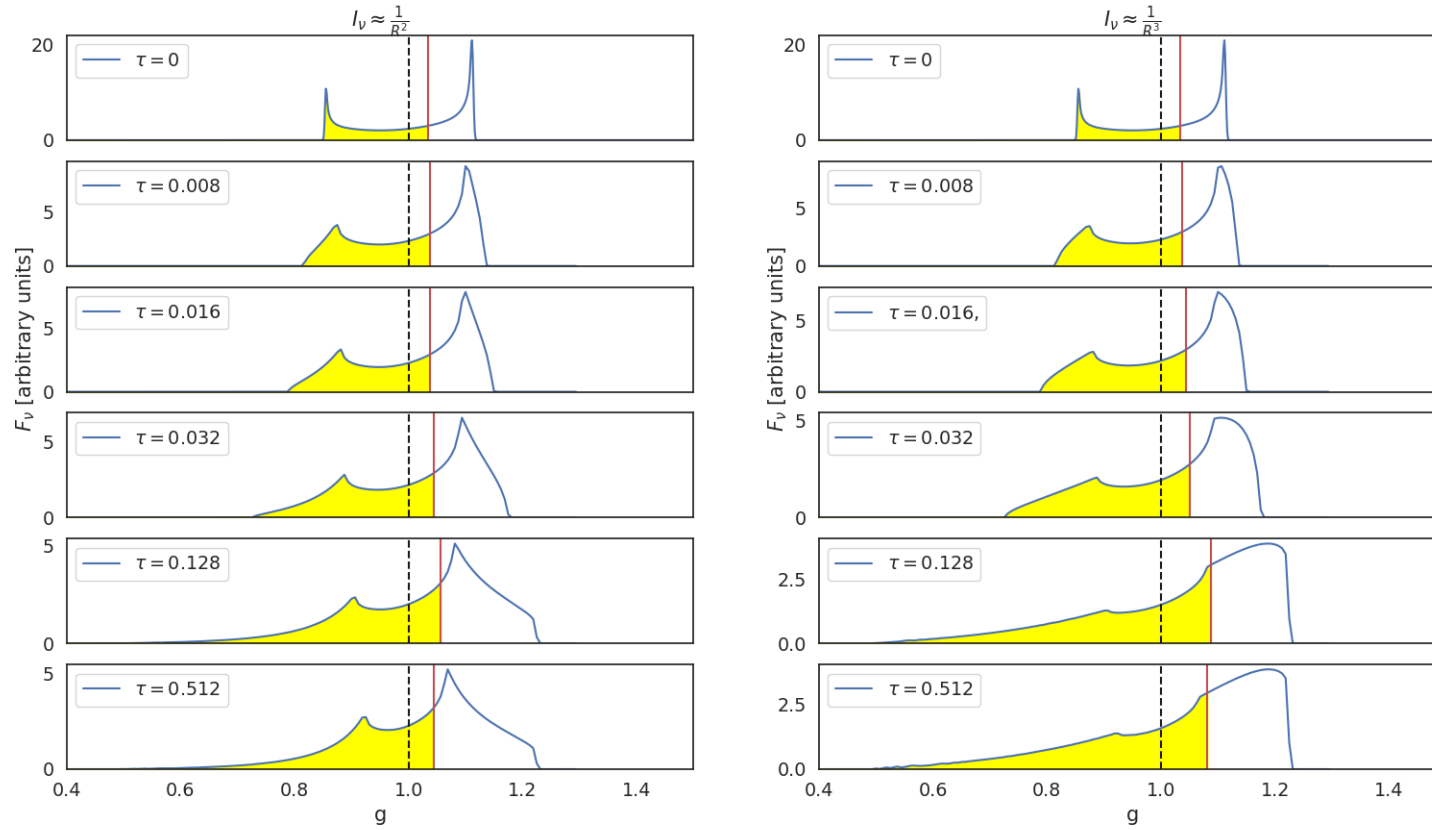
Figure 2.24: Spectral line profile evolution for the system set-up A with the inclination $I = 60$ deg, with the initial radiation intensity $I_\nu \approx \frac{1}{R^2}$ (left panel) and $I_\nu \approx \frac{1}{R^3}$ (right panel). Black dotted line marks the intrinsic frequency, red line marks the centroid energy of a given spectral line.
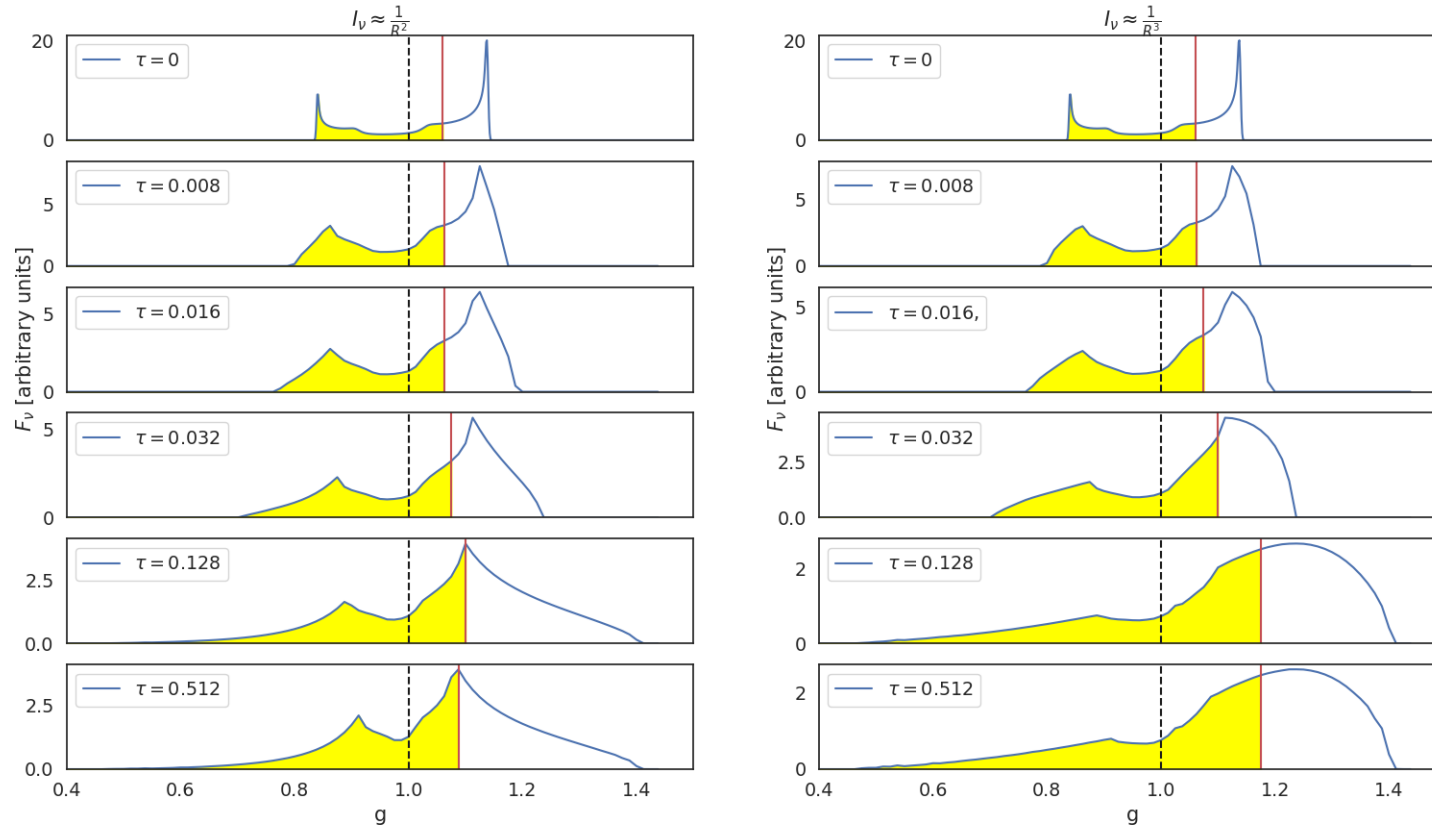
Figure 2.25: Spectral line profile evolution for the system set-up A with the inclination $I = 85$ deg, with the initial radiation intensity $I_\nu \approx \frac{1}{R^2}$ (left panel) and $I_\nu \approx \frac{1}{R^3}$ (right panel). Black dotted line marks the intrinsic frequency, red line marks the centroid energy of a given spectral line.

The spectral line shapes change drastically between the dimensionless time interval $\tau = 0$ and $\tau = 0.008$. The Figures 2.14, 2.15 and 2.16 with the initial mass ring located at $R = 12.8R_{\mathrm{g}}$ show such a behaviour in contrast with the remaining Figures 2.17 – 2.25 with their initial mass rings located farther away ($R = 23.6, 37.5$ and $45.4R_{\mathrm{g}}$). Let us note that the time parametrization we are using is guided by the equation (1.47). Using the equation (1.47) we calculated the time values of t for the given initial mass ring to evolve corresponding to the dimensionless time τ (see Table 2.3). We notice that the sudden changes in the spectral line shape 2.14, 2.15 and 2.16 compared to the remaining ones are caused by the fact that the initial mass ring is located close to its respective super-massive black hole and therefore the system evolves much faster than the systems with a less compact central body.

We calculated the position of the half of the energy of each spectral line profile in each system set-up during its evolution. In the context of spectral line profiles we call this position the centroid energy and mark it by a red line. We observe that the spectral line profiles assuming the source inclination $I = 35$ deg but different position of the initial mass ring have more than half of its energy redshifted (see Figures 2.14, 2.17, 2.20 and 2.23) during all of their evolution cycle ($\tau \in [0, 0.512]$). The remaining Figures showing the spectral line profile with the radiation source being inclined as $I = 60$ or 85 deg show that more than half of the energy is blueshifted during all of their evolution cycle ($\tau \in [0, 0.512]$).

With the help of our results from section 2.4 we can approximately identify the changes in different parameters. We can definitely see that the more the spectral line profile of the initial mass ring and the spectral line profile from the evolved accretion disc are shifted the higher is the inclination of the radiation source. As we are increasing the value of the tidal radius R_{tidal} we see that the evolved accretion disc stretches farther and farther away, see Table 2.2, as calculated by the numerical integration of the equation (1.40). Therefore we observe the spectral line's tendency to approach the intrinsic radiation frequency as the outer radius of the accretion disc R_{outer} grows with the increasing value of the dimensionless time τ, especially in case of the initial radiation intensity $I_\nu \approx \frac{1}{R^2}$. We also notice the influence of changing the value of the inner radius of the accretion disc R_{inner}. These changes project mostly in the cases with the initial radiation intensity as $I_\nu \approx \frac{1}{R^3}$ into the changes of the wing shape of a given spectral line profile. Comparing then the spectral line profiles having the same inclination and the initial mass ring position we notice that once reaching a certain dimensionless time τ during its evolution the shape of the wing stops changing. That is caused by the fact we set the lowest possible value for the radius of the accretion disc to be the ISCO radius $R_{\mathrm{ISCO}} = 6R_{\mathrm{g}}$.

Table 2.3: Viscous timescales for system set-up A, B, C and D

τ	D	C	B	A
	$t[yr]$	$t[yr]$	$t[yr]$	$t[yr]$
0.008	1821.7	2557.9	3194.5	3628.7
0.016	3643.5	5115.8	6288.9	7257.3
0.032	7286.9	10231.6	12777.8	14514.7
0.128	29147.6	40926.3	51111.2	58058.7
0.512	116590.4	163705.3	204444.9	232234.7

3. Conclusions and future prospects

We have studied the time evolution of the spectral line profiles (not taking into account the continuum) originating from the accretion disc which had developed as a result of the angular momentum transfer out of an initial mass ring. The predicted evolution of spectral line profile is expected to emerge in future observations of TDEs in active galaxies. In our toy-model the initial mass ring was located at the tidal radius given as (1.7) created by a tidal disruption of a solar-type star passing by a super-massive black hole. Also we assumed the whole system to be immersed in a high-energy medium (corona) surrounding the inner parts of the galactic centre.

To infer the constraints on the changing size of the evolving accretion disc we numerically solved the equation (1.40) (see Figure 2.1) where we compared the numerical and analytical solution given as (1.46) (see Figure 2.2 – 2.5) with the boundary condition $\Sigma(R_{\mathrm{ISCO}} = 0, t) = \Sigma(R_{\mathrm{outer}}, t) = 0$. We have also addressed the position of the median of mass in the accretion disc as it evolved for two different boundary conditions $\Sigma(R_{\mathrm{ISCO}} = 0, t) = \Sigma(R_{\mathrm{outer}}, t) = 0$ and $\Sigma(R_{\mathrm{ISCO}} = 6R_{\mathrm{g}}, t) = \Sigma(R_{\mathrm{outer}}, t) = 0$ (see Figure 2.6 and 2.7) and compared them based on the median position in the final form of the accretion disc (see Figure 2.8). In section 2.4 we present the spectral line profiles for rotating rings in Newtonian (see Figure 2.9), special relativistic (see Figure 2.10) and general relativistic approximation (see Figures 2.11 and 2.12) as well as the spectral line profiles of accretion discs in general relativistic approximation (see Figure 2.13) complemented by corresponding analysis.

The Figures 2.14 – 2.25 show the spectral line profile evolution and their centroid energy for a different system set-up (see Table 2.1) coming from the evolving accretion disc changing its size (see Table 2.2), taking into account the boundary condition $\Sigma(R_{\mathrm{ISCO}} = 6R_{\mathrm{g}}, t) = \Sigma(R_{\mathrm{outer}}, t) = 0$.

The Figures 2.20 – 2.22 show the spectral line profile evolution in system that involves the central object with the mass of $4 \times 10^6 M_{\odot}$ which is similar to that of Sagittarius A*, i.e. the super-massive black hole in our Galaxy centre (e.g. [Boehle et al., 2016]).

The future prospects of this study would be to look for the TDEs that might have an energy excess resembling that of Fe Kα emission line in the spectra in active galaxies and to compare it with the modeled spectra. In the future work it will be necessary to use a more general form of the redshift factor and the accretion disc evolution based on the Kerr or Kerr-Newmann metric.

References

G. T. Bath and J. E. Pringle. The evolution of viscous discs. I - Mass transfer variations. *Monthly Notices of the Royal Astronomical Society*, 194:967–986, March 1981. doi: 10.1093/mnras/194.4.967. URL `http://adsabs.harvard.edu/abs/1981MNRAS.194..967B`.

A. Boehle, A. M. Ghez, R. Schödel, L. Meyer, S. Yelda, S. Albers, G. D. Martinez, E. E. Becklin, T. Do, J. R. Lu, K. Matthews, M. R. Morris, B. Sitarski, and G. Witzel. An Improved Distance and Mass Estimate for Sgr A* from a Multistar Orbit Analysis. *The Astrophysical Journal*, 830(1):17, Oct 2016. doi: 10.3847/0004-637X/830/1/17. URL `https://ui.adsabs.harvard.edu/abs/2016ApJ...830...17B`.

H. Bondi. On spherically symmetrical accretion. *Monthly Notices of the Royal Astronomical Society*, 112:195, 1952. doi: 10.1093/mnras/112.2.195. URL `http://adsabs.harvard.edu/abs/1952MNRAS.112..195B`.

J. R. Cummings, S. D. Barthelmy, A. P. Beardmore, D. N. Burrows, S. Campana, V. D'Elia, P. A. Evans, N. Gehrels, J. M. Gelbord, C. Guidorzi, S. T. Holland, E. A. Hoversten, J. A. Kennea, H. A. Krimm, O. M. Littlejohns, R. Margutti, F. E. Marshall, A. Melandri, C. Pagani, K. L. Page, D. M. Palmer, P. Romano, M. H. Siegel, E. Sonbas, R. L. C. Starling, G. Stratta, G. Tagliaferri, and E. Troja. GRB 110328A: Swift detection of a burst. *GRB Coordinates Network, Circular Service, No. 11823, #1 (2011)*, 11823, March 2011. URL `http://adsabs.harvard.edu/abs/2011GCN.11823....1C`.

M. Dovčiak, V. Karas, and T. Yaqoob. An Extended Scheme for Fitting X-Ray Data with Accretion Disk Spectra in the Strong Gravity Regime. *The Astrophysical Journal Supplement Series*, 153:205–221, July 2004. doi: 10.1086/421115. URL `http://adsabs.harvard.edu/abs/2004ApJS..153..205D`.

Event Horizon Telescope Collaboration, K. Akiyama, A. Alberdi, W. Alef, K. Asada, R. Azulay, A.-K. Baczko, D. Ball, M. Baloković, J. Barrett, and et al. First M87 Event Horizon Telescope Results. V. Physical Origin of the Asymmetric Ring. *The Astrophysical Journal Letters*, 875:L5, April 2019. doi: 10.3847/2041-8213/ab0f43. URL `http://adsabs.harvard.edu/abs/2019ApJ...875L...5E`.

A. C. Fabian, M. J. Rees, L. Stella, and N. E. White. X-ray fluorescence from the inner disc in Cygnus X-1. *Monthly Notices of the Royal Astronomical Society*, 238:729–736, May 1989a. doi: 10.1093/mnras/238.3.729. URL `http://adsabs.harvard.edu/abs/1989MNRAS.238..729F`.

A. C. Fabian, M. J. Rees, L. Stella, and N. E. White. X-ray fluorescence from the inner disc in Cygnus X-1. *Monthly Notices of the Royal Astronomical Society*, 238:729–736, May 1989b. doi: 10.1093/mnras/238.3.729. URL `http://adsabs.harvard.edu/abs/1989MNRAS.238..729F`.

J. Frank, A. King, and D. Raine. Accretion Power in Astrophysics. *Cambridge University Press; 3 edition*, 2002.

O. K. Guseinov and Y. B. Zel'dovich. Collapsed Stars in Binary Systems. *Soviet Astronomy*, 10:251, oct 1966. URL `http://adsabs.harvard.edu/abs/1966SvA....10..251G`.

J. G. Hills. Possible power source of Seyfert galaxies and QSOs. *Nature*, 254:295–298, March 1975. doi: 10.1038/254295a0. URL `http://adsabs.harvard.edu/abs/1975Natur.254..295H`.

F. Hoyle and R. A. Lyttleton. On the accretion theory of stellar evolution. *Monthly Notices of the Royal Astronomical Society*, 101:227, 1941. doi: 10.1093/mnras/101.4.227. URL `http://adsabs.harvard.edu/abs/1941MNRAS.101..227H`.

I. Hubený and D. Mihalas. Theory of Stellar Atmospheres. *PRINCETON SERIES IN ASTROPHYSICS*, page 72, 2014.

E. Kara, J. M. Miller, C. Reynolds, and L. Dai. Relativistic reverberation in the accretion flow of a tidal disruption event. *Nature*, 535:388–390, July 2016. doi: 10.1038/nature18007. URL `http://adsabs.harvard.edu/abs/2016Natur.535..388K`.

D. Kazanas, K. Fukumura, E. Behar, I. Contopoulos, and C. Shrader. Toward a Unified AGN Structure. *The Astronomical Review*, 7(3):92–123, July 2012. doi: 10.1080/21672857.2012.11519707. URL `http://adsabs.harvard.edu/abs/2012AstRv...7c..92K`.

R. P. Kerr. Gravitational Field of a Spinning Mass as an Example of Algebraically Special Metrics. *Physical Review Letters*, 11:237–238, September 1963. doi: 10.1103/PhysRevLett.11.237. URL `http://adsabs.harvard.edu/abs/1963PhRvL..11..237K`.

Y. Kojima. The effects of black hole rotation on line profiles from accretion discs. *Monthly Notices of the Royal Astronomical Society*, 250:629–632, June 1991. doi: 10.1093/mnras/250.3.629. URL `http://adsabs.harvard.edu/abs/1991MNRAS.250..629K`.

S. Komossa. Tidal disruption of stars by supermassive black holes: Status of observations. *Journal of High Energy Astrophysics*, 7:148–157, September 2015. doi: 10.1016/j.jheap.2015.04.006. URL `http://adsabs.harvard.edu/abs/2015JHEAp...7..148K`.

A. Laor. Line profiles from a disk around a rotating black hole. *The Astrophysical Journal*, 376:90–94, July 1991. doi: 10.1086/170257. URL `http://adsabs.harvard.edu/abs/1991ApJ...376...90L`.

D. Lin, J. Guillochon, S. Komossa, E. Ramirez-Ruiz, J. A. Irwin, W. P. Maksym, D. Grupe, O. Godet, N. A. Webb, D. Barret, B. A. Zauderer, P.-A. Duc, E. R. Carrasco, and S. D. J. Gwyn. A likely decade-long sustained tidal disruption event. *Nature Astronomy*, 1:0033, February 2017. doi: 10.1038/s41550-016-0033. URL `http://adsabs.harvard.edu/abs/2017NatAs...1E..33L`.

F. K. Liu, S. Li, and X. Chen. Interruption of Tidal-Disruption Flares by Supermassive Black Hole Binaries. *The Astrophysical Journal Letters*, 706: L133–L137, November 2009. doi: 10.1088/0004-637X/706/1/L133. URL `http://adsabs.harvard.edu/abs/2009ApJ...706L.133L`.

F. K. Liu, S. Li, and S. Komossa. A Milliparsec Supermassive Black Hole Binary Candidate in the Galaxy SDSS J120136.02+300305.5. *The Astrophysical Journal*, 786:103, May 2014. doi: 10.1088/0004-637X/786/2/103. URL `http://adsabs.harvard.edu/abs/2014ApJ...786..103L`.

Z. Liu, W. Yuan, Y. Lu, F. Carrera, S. Falocco, and X. Dong. Dependence of the broad Fe Kα line on the physical parameters of AGN. *The X-ray Universe 2017*, page 293, October 2017. URL `http://adsabs.harvard.edu/abs/2017xru..conf..293L`.

J.-P. Luminet and B. Pichon. Tidal pinching of white dwarfs. , 209:103–110, January 1989. URL `http://adsabs.harvard.edu/abs/1989A%26A...209..103L`.

J. Magorrian, S. Tremaine, D. Richstone, R. Bender, G. Bower, A. Dressler, S. M. Faber, K. Gebhardt, R. Green, C. Grillmair, J. Kormendy, and T. Lauer. The Demography of Massive Dark Objects in Galaxy Centers. *The Astronomical Journal*, 115:2285–2305, June 1998. doi: 10.1086/300353. URL `http://adsabs.harvard.edu/abs/1998AJ....115.2285M`.

Ch. W. Misner, K. S. Thorne, and Wheeler J. A. *Gravitation*, pages 875–876, 1973. San Francisco.

M. Montesinos Armijo and J. A. de Freitas Pacheco. Tidal Disruption Flares: The Accretion Disk Phase. *The Astrophysical Journal*, 736:126, August 2011. doi: 10.1088/0004-637X/736/2/126. URL `http://adsabs.harvard.edu/abs/2011ApJ...736..126M`.

E. T. Newman, E. Couch, K. Chinnapared, A. Exton, A. Prakash, and R. Torrence. Metric of a Rotating, Charged Mass. *Journal of Mathematical Physics*, 6 (6):918–919, 1965. doi: 10.1063/1.1704351. URL `https://doi.org/10.1063/1.1704351`.

G. Nordström. On the Energy of the Gravitational Field in Einstein's Theory. *Verhandl. Koninkl. Ned. Akad. Wetenschap., Afdel. Natuurk., Amsterdam*, 26: 1201–1208, 1918.

I. D. Novikov and Ya. Zel'dovich. PHYSICS OF RELATIVISTIC COLLAPSE. *Nuovo Cimento, Suppl. (1)*, 4:810–27, January 1966.

T. Pecháček, M. Dovčiak, and V. Karas. The relativistic shift of spectral lines from black-hole accretion discs. pages 137–141, December 2005. URL `http://adsabs.harvard.edu/abs/2005ragt.meet..137P`.

M. J. Rees. Tidal disruption of stars by black holes of 10 to the 6th-10 to the 8th solar masses in nearby galaxies. *Nature*, 333:523–528, June 1988. doi: 10.1038/333523a0. URL `http://adsabs.harvard.edu/abs/1988Natur.333..523R`.

H. Reissner. Über die Eigengravitation des elektrischen Feldes nach der Einsteinschen Theorie. *Annalen der Physik*, 50:106–120, 1916. doi: 10.1002/andp. 19163550905.

R. D. Saxton, A. M. Read, P. Esquej, S. Komossa, S. Dougherty, P. Rodriguez-Pascual, and D. Barrado. A tidal disruption-like X-ray flare from the quiescent galaxy SDSS J120136.02+300305.5. , 541:A106, May 2012. doi: 10.1051/ 0004-6361/201118367. URL http://adsabs.harvard.edu/abs/2012A%26A. ..541A.106S.

S. A. Shapiro and S. L Teukolsky. Black Holes, White Dwarfs, and Neutron Stars: The Physics of Compact Objects. *WILEY-VCH Verlag GmbH Co. KGaA*, pages 73–101, 1983.

I. S. Shklovsky. On the Nature of the Source of X-Ray Emission of Sco XR-1. *The Astrophysical Journal*, 148:L1, apr 1967. doi: 10.1086/180001. URL http://adsabs.harvard.edu/abs/1967ApJ...148L...1S.

N. C. Stone. The Tidal Disruption of Stars by Supermassive Black Holes An Analytic Approach. *Springer Theses*, pages 1–12, 2015. doi: 10.1007/ 978-3-319-12676-0.

N. C. Stone, M. Kesden, R. M. Cheng, and S. van Velzen. Stellar tidal disruption events in general relativity. *General Relativity and Gravitation*, 51:30, February 2019. doi: 10.1007/s10714-019-2510-9.

Y. Tanaka, K. Nandra, A. C. Fabian, H. Inoue, C. Otani, T. Dotani, K. Hayashida, K. Iwasawa, T. Kii, H. Kunieda, F. Makino, and M. Matsuoka. Gravitationally redshifted emission implying an accretion disk and massive black hole in the active galaxy MCG-6-30-15. *Nature*, 375:659–661, June 1995. doi: 10.1038/375659a0. URL http://adsabs.harvard.edu/abs/1995Natur. 375..659T.

D. Zwillinger. CRC standard mathematical tables and formulae. *Chapman and Hall/CRC, Chapter 5.11*, 2002.

List of Figures

List of Tables

List of Abbreviations

AGN – active galactic nucleus
ISCO – innermost stable circular orbit
TDE – tidal disruption event

A. Appendix

A.1 Details of numerical calculations and plot resolution

In order to obtain the numerical solution to the equation (1.40) we first had to choose the appropriate value of the kinematic viscosity, in our case the value of C_ν, as we defined in the equation (2.15). Then after calculating the respective tidal radius via the equation (1.7) we were able to calculate the time t using the dimensionless time τ and the equation (1.47). We had to pick a reasonable Δx and Δt in order to satisfy the von Neumann stability criterion (2.12). One can notice that the Figure 2.6 and 2.7 do not have the same resolution. This is caused by the fact that these are numerical solutions having different boundary conditions, $\Sigma(R_{\text{inner}} = 0, t) = \Sigma(R_{\text{outer}}, t) = 0$ and $\Sigma(R_{\text{ISCO}} = 6R_{\text{g}}, t) = \Sigma(R_{\text{outer}}, t) = 0$ respectively. The numerical solution depicted in the Figure 2.7 leaves out the x values close to zero as we force the surface density to be zero at the ISCO radius R_{ISCO} which makes it possible to choose higher spatial splitting than in case of the numerical solution depicted in the Figure 2.6 not ignoring x values close to zero.

For the spectral line profile calculation we used the delta distribution approximation in form (2.21). We have chosen the parameter $a = 0.01$ for all spectral line profile models except for the spectral line profile of the rotating ring in Newtonian approximation (see Figure 2.9) where we chose $a = 0.001$. To make the spectral line profile calculations stable and relatively short we kept diminishing the infinitesimal contributions in radial dR and azimuthal direction $d\varphi$. Another reason was the effort to partially dispose of the numerical noise, especially in case of the accretion discs with the biggest covered area or the biggest inclination (see the middle and the last two plots in the Figure 2.13). We have tried to choose an appropriate plot resolution given the spectral line profile, i.e. the more "spiky" the spectral line profile's peaks the higher the plot resolution et vice versa.

The values for physical constants that we took into account are as follows: the gravitational constant $G = 6.67 \times 10^{-11}$ m^3.kg^{-1}.s^{-2}, the Stefan-Boltzmann constant $\sigma = 5.67 \times 10^{-8}$ W.m^{-2}.K^{-4}, the semi-empirical α constant as $\alpha \approx 1$, the speed of light $c = 3 \times 10^8$ m.s^{-1}, the Boltzmann constant $k_{\text{b}} = 1.38 \times 10^{-23}$ J.K^{-1}, the mean molecular mass $\mu \approx 1$, the mass of a proton $m_{\text{p}} = 1.67 \times 10^{-27}$ kg, the solar mass constant $M_\odot = 2 \times 10^{30}$ kg and the solar radius $R_\odot \approx 7 \times 10^8$ m.